Preflight and In-Flight Calibration of the Spectral Profiler on Board SELENE (Kaguya)

Satoru Yamamoto, Tsuneo Matsunaga, Yoshiko Ogawa, Ryosuke Nakamura, Yasuhiro Yokota, Makiko Ohtake, Junichi Haruyama, Tomokatsu Morota, Chikatoshi Honda, Takahiro Hiroi, and Shinsuke Kodama

***Abstract*—The Spectral Profiler (SP) is a visible–near infrared spectrometer on board the Japanese Selenological and Engineering Explorer, which was launched in 2007 and observed the Moon until June 2009. The SP consists of two gratings and three linear-array detectors: VIS (0.5–1.0 μm), NIR 1 (0.9–1.7 μm), and NIR 2 (1.7–2.6 μm). In this paper, we characterize the radiometric and spectral properties of VIS and NIR 1 using in-flight observational data as well as preflight data derived in laboratory experiments using a calibrated integrating sphere. We also proposed new methods for radiometric calibration, specifically methods for nonlinearity correction, wavelength correction, and the correction of the radiometric calibration coefficients affected by the water vapor. After all the corrections, including the photometric correction, we obtained the reflectance spectra for the lunar surface. Finally, we examined the stability of the SP using the SP data near the Apollo 16 landing site observed at four different times. The difference in reflectance among these four observations was less than $\sim \pm 1\%$ for most of the bands, suggesting that the degradation of the SP is not significant over the mission period.**

***Index Terms*—Infrared spectroscopy, Moon, remote sensing, spectral analysis, spectroscopy.**

I. Introduction

THE Japan Aerospace Exploration Agency (JAXA) launched the SELenological and ENgineering Explorer (SELENE/Kaguya) spacecraft in September 2007 and observed the Moon until June 2009. The Spectral Profiler (SP) [2], [3] on board SELENE is an optical subsystem of the Lunar Imager/Spectrometer [4]. The SP consists of two gratings and three linear-array detectors: VIS, NIR 1, and NIR 2. During the mission, from November 2007 to June 2009, the SP obtained continuous spectral reflectance data for more than 68 million points on the Moon.

The SP is designed to clarify the global distribution of mineral composition on the surface of the Moon, which is thought to be a key factor in revealing the overall composition and the evolution of the lunar crust and mantle [3], [5], [6]. For the identification of mineral composition from spectral reflectance data, it is important to characterize the behavior of the instruments used based on both preflight experiments and in-flight observations over the mission period. This requires a detailed evaluation of various calibration processes: dark signal, nonlinear response, wavelength shift, correction of the radiometric calibration coefficients (RCCs) in the water-vapor-affected spectral region, and gap adjustment between detectors. In addition, we need to examine the stability of the radiometric calibration during the mission period.

In this paper, we characterize the radiometric and spectral properties of the SP and propose new methods for radiometric calibration, specifically methods for nonlinearity correction, wavelength correction, and the correction of RCCs affected by the atmosphere. Note that the focus of this paper is on radiometric calibration to derive the reflectance for the mineralogical survey, and absolute radiometric calibration will be performed in future studies. Since the analysis of the NIR 2 data is still incomplete, this paper considers only the VIS and NIR 1 data.

In Section II, we first give the overview of the SP instrument and its mission. We then evaluate the radiometric calibration for SP data in Section III. Radiance conversion is discussed in Section IV, and the reflectance data, with the photometric correction, are discussed in Section V. Finally, in Section VI, we examine the stability of the radiometric calibration during the mission period using the SP data near the Apollo 16 landing site observed at four different times.

II. SP Instrument and Mission Overview

Fig. 1 shows a schematic diagram of the SP and its optical configuration. The SP is a Cassegrain line spectral profiler, which measures a spectrum for each SP footprint. This consists of one reflective foreoptics (focal length: 125 mm, F: 3.9), two plane gratings, and three linear-array detectors, i.e., VIS, NIR 1, and NIR 2. The instrument characteristics are summarized in Table I. The light focused by the foreoptics passes through the narrow slit and is separated by two spectrometers (SP-VIS and SP-NIR spectrometers). The VIS detector is a 128-pixel Si p-i-n photodiode linear array detector with a pixel size of 50×500 μm. We used 84 contiguous pixels out of 128 pixels,

Manuscript received December 6, 2010; revised March 2, 2011 and April 4, 2011; accepted April 11, 2011. Date of publication May 31, 2011; date of current version October 28, 2011. This work was supported in part by a Grant-in-Aid for Young Scientist (B)(20740249)(S.Y.) and KAKENHI (20540416)(J.H.) from the Japan Society for the Promotion of Science.

S. Yamamoto, T. Matsunaga, and Y. Yokota are with the Center for Global Environmental Research, National Institute for Environmental Studies, Tsukuba 305-8506, Japan (e-mail: yamamoto.satoru@nies.go.jp).

Y. Ogawa and C. Honda are with the ARC-Space/Research Center for Advanced Information Science and Technology (CAIST), The University of Aizu, Aizu-Wakamatsu 965-8580, Japan.

R. Nakamura and S. Kodama are with the Information Technology Research Institute, National Institute of Advanced Industrial Science and Technology, Tsukuba 305-8568, Japan.

M. Ohtake and J. Haruyama are with the Institute of Space and Astronautical Science, Japan Aerospace Exploration Agency, Sagamihara 252-5210, Japan.

T. Morota is with RISE Project, National Astronomical Observatory of Japan, Mitaka 181-8588, Japan.

T. Hiroi is with the Department of Geological Sciences, Brown University, Providence, RI 02912 USA.

Digital Object Identifier 10.1109/TGRS.2011.2144990

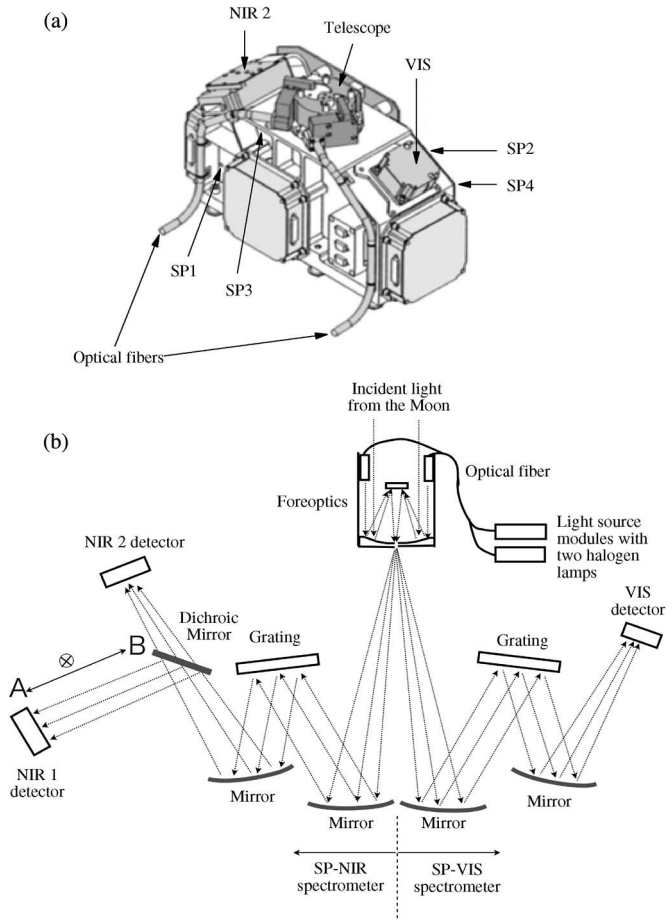

Fig. 1. (a) Schematic diagram of the SP. Thermometers SP1, SP2, SP3, and SP4 (indicated by arrows) are glued to the inside wall of the spectrometer body. (b) Configuration of the SP optical system. In order to avoid confusion, in this figure, all of the optical systems are drawn in the same plane, although the actual direction between the dichroic mirror and NIR 1 detector (A–B in this figure) is perpendicular to this figure.

TABLE I
INSTRUMENT'S CHARACTERISTICS

Telescope	Cassegrain
Spectrometer design	Czerny-Turner
Focal length	125 mm
F number	3.9

which cover the wavelength range of $\lambda = 512.6-1010.7$ nm with a sampling interval of 6 nm. The light sent to the SP-NIR spectrometer is split by a dichroic mirror into the NIR 1 and NIR 2 detectors. These detectors are the same as the 128-pixel InGaAs detectors with a pixel size of 50×200 μm. We also used 100 (NIR 1) and 112 (NIR 2) contiguous pixels out of the 128 pixels, which cover the wavelength ranges of $\lambda =$ 883.5–1676.0 nm and $\lambda = 1,702.1$–2587.9 nm, respectively, with a spectral resolution of 8 nm. The NIR 2 detector is cooled using a three-stage Peltier device cooled to 243 K to reduce the thermal noise. Note that the preflight calibration showed that the band number $n = 100$ ($\lambda = 1003.6$ nm) responds abnormally.

TABLE II
NAMING CONVENTION OF SP DATA PRODUCTS

Level 2A (L2A)	Raw data
Level 2B (L2B)	Radiance and diffuse spectral reflectance
Level 2C (L2C)	Radiance and photometrically corrected reflectance

The SP has an onboard calibration apparatus that consists of two lighting modules attached to the SP foreoptics and a light source module in the spacecraft with two halogen lamps (see Fig. 1). The two modules are connected by optical fibers (of 1 m in length), whose one side is bare and another side is equipped with a collimator. The power of the halogen lamps is 9 W, and the sources are stabilized in voltage. This onboard calibration apparatus was used for the short-term monitoring of the instrument, including ground testing phase, in which the degradation of this apparatus is not critical. Since the assessment of the instrument response stability based on the onboard calibration apparatus is still ongoing, we will not treat this in this paper.

As will be shown later, the signal measured by the SP sometimes depends on the temperature of the instrument. Based on an analysis of the telemetry information of 14 thermometers, we use the SP1 thermometer [see Fig. 1(a)], which shows the best correlations with the dark output of NIR 1 and with the wavelength shift in VIS.

The field of view of the SP is 0.23° or $\sim$500 m on the lunar surface at the planned highest altitude of 130 km. The average altitude during the nominal mission period is $\sim$100 km. The instantaneous field of view (IFOV) is $\sim 50 \times 500$ m. The along-track sampling interval is 90 ms, which corresponds to 140 m on the lunar surface (at a ground speed of 1.6 km s^{-1}). For one observational spectrum, four 90-ms data are averaged before sending information to SELENE's data recorder, resulting in an $\sim$500-m observational footprint. We can choose an integration time τ in each 90-ms data of either $\tau = 26$ ms (short exposure mode) or $\tau = 77$ ms (long exposure mode). The data are packed and transmitted to SELENE's data recorders after 16-b analog-to-digital conversion.

The naming convention of the SP data product is summarized in Table II. A Level 2A (L2A) data product, processed by the SELENE Operation and Analysis Center at the Institute of Space and Astronautical Science, was radiometrically calibrated to produce Level 2B1/2B2 (L2B1 and L2B2) products, which give the radiance and diffuse reflectance (radiance factor without photometric correction). The L2B1 data contain all of the data in one revolution. For the case of the L2B2 data, the L2B1 data are separated to a scene accompanied with an image obtained by the Multiband Imager (MI) or the Terrain Camera (TC) on board SELENE [4]. A Level 2C (L2C) product provides the photometrically corrected reflectance with the accompanied image obtained by MI or TC, which locates the positions of the SP footprints on the image based on the along-track radiance correlation between the TC/MI and the SP.

Fig. 2(a) shows how the SP measures the lunar surface in one orbit of SELENE around the Moon. At each revolution, the SP starts to observe the lunar surface at the night side of the Moon, where the observational line number L is defined as

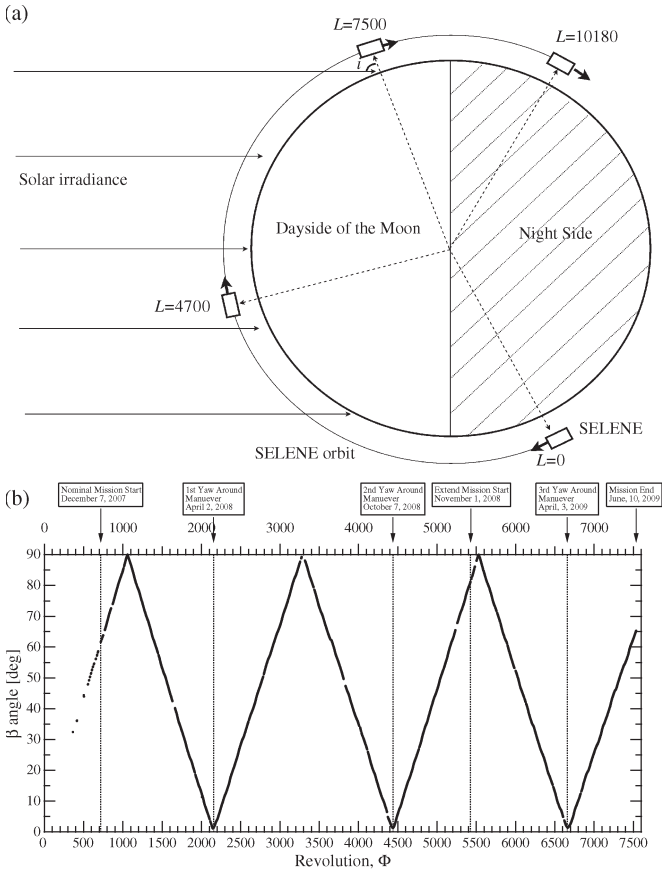

Fig. 2. (a) Schematic diagram of the positions of SELENE, the SP observational footprint, the Moon, and the solar irradiance. Here, i is the solar incident angle, where $i = 0^\circ$ corresponds to the normal direction to the surface. In addition, L is the observational line number. This is the case for which $\beta = 0^\circ$, which occurs when the orbital plane of SELENE around the Moon is the same as the scattering plane. (b) The relation between the β angle and the SELENE revolution Φ, where the β angle is defined as the solar incidence angle at the equator.

$L = 0$. The SP then continues to collect data across the day side until SELENE enters the night side of the Moon. The typical total line number for one revolution ranges from 10 000 to 20 000. In this figure, we also define the solar incident angle i, which is measured from the normal direction to the surface.

Fig. 2(b) shows the temporal changes of the solar incident angle β at the equator, which is one of the important factors affecting the thermal condition of the SP. In order to control its thermal condition, SELENE changed its orientation with respect to the Sun three times (by yaw around maneuver) at $\beta \sim 0^\circ$: April 2, 2008, October 7, 2008, and April 3, 2009. The nominal mission started at a revolution number of $\Phi = 719$ (December 7, 2007). The revolution of the nominal mission ranges from $\Phi = 719$ to 5426, followed by the extended mission period.

For most observations, the direction from the SP to the SP boresight is approximately equal to the normal direction to the surface, which is regarded as the surface of the virtual sphere of the Moon. As special observations, four Apollo 16 landing site observations were conducted at six-month intervals (see Section VI). In each observation, SELENE changed its attitude to obtain data at a phase angle of $g \sim 30^\circ$. Permanent failure of the reaction wheel of the SELENE spacecraft occurred on

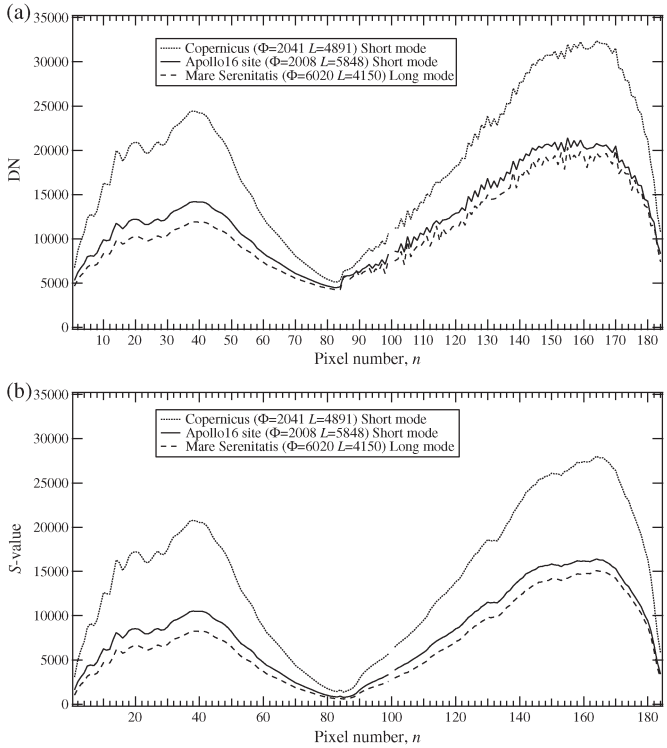

Fig. 3. (a) Original DN and (b) S-values, which are the difference between the original DN and the dark DN, for the central peak of Copernicus crater ($\Phi = 2041$ and $L = 4891$), near the Apollo 16 landing site ($\Phi = 2008$ and $L = 5848$), and at Mare Serenitatis ($\Phi = 6020$ and $L = 4150$). Here, the DN at $n = 100$ is not shown because the preflight calibration showed that this band responds abnormally.

December 26, 2008. After this failure, the SELENE spacecraft was controlled by thrusters. In this situation, the attitude of the SELENE spacecraft sometimes became unsteady, resulting in an unstable optical geometric condition for the observation.

The preflight calibration experiments were conducted at the JAXA Tsukuba Space Center. These experiments include the following: 1) determination of the RCCs to derive the radiance from the signal data using a calibrated integrating sphere; 2) nonlinear response calibration, as will be described in Section III-B; and 3) the center wavelengths of all detector elements were determined using a monochromator during preflight calibration experiments. A more detailed description of the experiments is given in [7].

III. Radiometric Calibration for Radiance

Fig. 3(a) shows the original digital number (DN) obtained at three reference sites. Radiometric calibration is needed in order to obtain the radiance I (W m^{-2} sr^{-1} μm^{-1}) from the original DN. Fig. 4 shows a flowchart of the radiometric calibration used to produce the SP L2B and L2C products: 1) removal of dark signal; 2) nonlinearity correction; 3) wavelength correction; 4) radiance conversion; and 5) gap adjustments between detectors. In the following, we discuss each procedure in detail.

A. Dark DN Determination

In this section, we investigate the characteristics of the dark output (dark DN) for VIS and NIR 1. Based on these

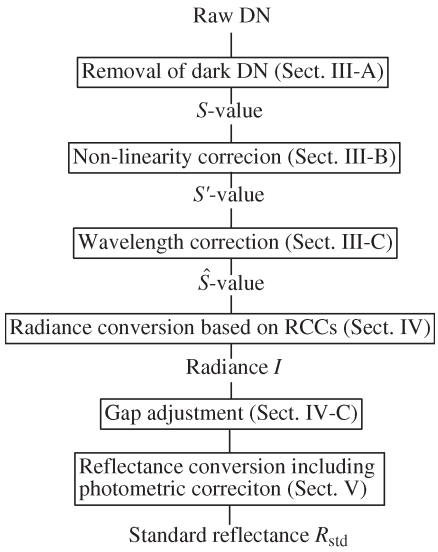

Fig. 4. Flowchart of the radiometric calibration of the SP.

characteristics, we propose methods by which to determine the dark DN for VIS and NIR 1 for each observation.

1) VIS: Since the SP does not have a shutter to cut the incidence light, we estimate the dark DN from the data obtained at the night side of the Moon. We first discuss how to determine the night side data for each revolution. Fig. 5(a) shows a temporal change of the DN with a band number $n = 32$ ($\lambda = 698.6$ nm) for one SP revolution. The bottom axis is the line number L, and the solar incidence angle i is indicated by the top axis. The DN with $L = 0$ to ~ 500 ($i > 90^\circ$) remains nearly constant ($\sim$3660 DN). Then, the DN rises abruptly at $L > \sim 500$ and increases with increasing L with a short time variation by topographical features illuminated by the Sun. After $L > \sim 10\,200$ ($i > 90^\circ$), the DN remains at a lower constant value ($\sim$3670 DN). Therefore, we consider that, when $i > 90^\circ$, the SP data correspond to the dark DN.

There are a few abrupt increases, even at $i > 90^\circ$, as shown in the insets in Fig. 5(a). This is due to the solar light reflected by local surface features at near-polar regions (e.g., a crater rim or a mountain). In addition, a slight increase in the DN is also observed at $i > \sim 96^\circ - 100^\circ$. After $i = 90^\circ$, as SELENE moves toward the night side, the bottom side of the SELENE body tilts toward the Sun (see Fig. 2). However, immediately after $i = 90^\circ$, the SELENE body is still outside the shadow region of the Moon, although the footprint of SP enters the night side of the Moon. The sunlight reflected by the bottom side of the body of SELENE might have entered through the foreoptics and affected the DN (stray light). We have also confirmed that, after SELENE enters completely the night side of the Moon (the solar incident angle $i > 109^\circ$), the dark DN decreases again.

In order to avoid the effects of light reflected by local surface features at polar regions and stray light, we propose the median value of the DN with $i > 90^\circ$ as the dark DN. Fig. 5(b) shows the histogram of the DN at $i > 90^\circ$. The difference between the DN at the peak and the median DN is $\sim$5 DN. This difference is $\sim$0.05% of the typical S-value of VIS [$\sim$10 000 DN; see Fig. 3(b)], where the S-value is defined as the difference between the original DN and the dark DN. Thus, in the proposed

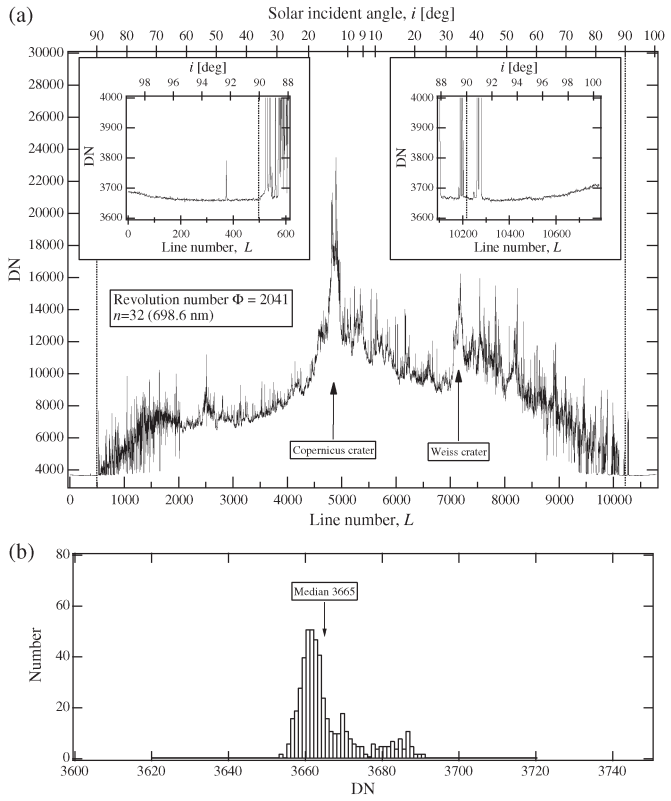

Fig. 5. (a) DN is plotted with respect to the line number L for $n = 32$ ($\lambda = 698.6$ nm). The revolution number is $\Phi = 2041$, when the SP passed over the central peaks of Copernicus crater at around $L \sim 4891$ and over the Wiess crater at $L \sim 7100$ to 7150. The corresponding i is also plotted with respect to the top axis. The vertical broken line indicates $i = 90^\circ$. The insets show the data for $L < 609$ and $L > 10\,100$ ($i > \sim 88^\circ$). (b) The histogram of DN for $i > 90^\circ$ (for $\Phi = 2041$).

method, the error for the removal of the dark DN is estimated to be 0.05% for the S-value of 10 000 DN. Since, for a single revolution, there are two conditions in which $i > 90^\circ$ (i.e., smaller and larger L), we average the two median values for one revolution.

In Fig. 6(a), the dark DN, which was obtained from the aforementioned method, is plotted with respect to n. The figure shows that the dark DN for VIS is nearly independent of n, although there is a jagged pattern (odd–even shape) between the odd and even pixel numbers. The cause of the jagged pattern is unknown, although there is a possibility that this may be introduced by the small differences in the offset between multiplexer stages connected at the odd and even pixels.

We next examine the temporal change of the dark DN. In Fig. 6(b), the average dark DN for $n = 1$ to 84 is plotted with respect to Φ. As shown in this figure, the dark DN decreases gradually with increasing Φ. We also plot the dark DN for the preflight calibrations in Fig. 6(b). The dark DN for the preflight calibrations of 3760 ± 5 DN is near to or slightly lower than the values of 3760–3780 DN measured at the first measurements after the launch ($\Phi = 294$–296). The dark DN may have become larger than the preflight value during the launch and then decreased owing to the long-term effects of space radiation or the degassing of some gases inside the spectrometer. However, we do not have any specific evidence for these long-term effects. This is not due to the thermal effect,

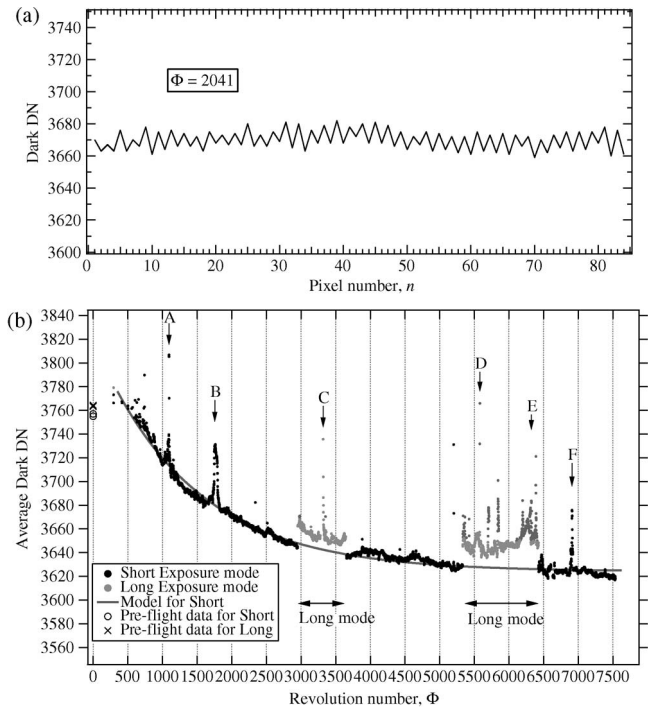

Fig. 6. (a) The dark DN is plotted with respect to n for VIS ($\Phi = 2041$). (b) Temporal change of the average dark DN for $n = 1$ to 84. The solid curve is the best fit curve for the short exposure mode: $D_{\rm vis} = 3624 + 195\exp(-0.000711\Phi)$.

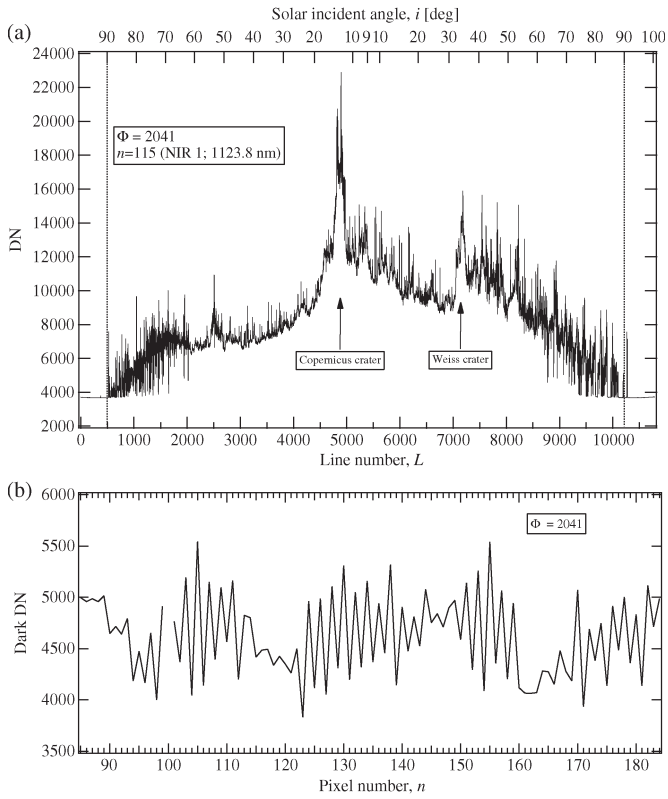

Fig. 7. (a) DN is plotted with respect to L for $n = 115$ (NIR 1 #31; $\lambda = 1123.8$ nm). The revolution number is $\Phi = 2041$. The corresponding i is also plotted with respect to the top axis. The vertical broken line indicates $i = 90^\circ$. (b) Dark DN is plotted with respect to n for (a).

because the temperature telemetry does not show such a long-term decrease.

We modeled the average dark DN ($D_{\rm vis}$) for the short exposure mode as

$$D_{\rm vis} = 3624 + 195\exp(-0.000711\Phi) \tag{1}$$

where the differences in $D_{\rm vis}$ among n (or the wavelength) are within 10 DN. This is $\sim$0.1% of the typical S-value of VIS ($\sim$10 000 DN). Equation (1) can be used for the production of L2B data from L2A data, which does not provide data for the DN at $i > 90^\circ$. Fig. 6(b) also shows that the dark DN for the long exposure mode ($\Phi = 3000$–3600 and 5300–6400) is slightly larger than that for the short exposure mode. We also use (1) to produce L2B data from L2A data, which does not provide data for the DN at $i > 90^\circ$, with the long exposure mode.

We find that there are short temporal increases in the average dark DN at several revolutions, e.g., $\Phi \sim 1100,\ 1800,\ 3300,\ \sim 5300$–$6400,$ and 6900. There are different reasons for these increases. First, at $\Phi \sim 1100,\ 3300,$ and 5550 [marked A, C, and D in Fig. 6(b)], the SP observes the region near the lunar terminator [i.e., higher β values ($\sim 90^\circ$)]. In these revolutions, the solar incident angle ranges from $i \sim 89^\circ$ to $\sim 91^\circ$. There are frequent abrupt increases in the DN due to the solar light reflected by the local surface features for $i = 90^\circ$ to 91°, thus causing an increase in the median value of the DN. Second, a significant number of the scattered data at $\Phi = 5300$–6400 and 6900 (marked E and F) may be related to trouble with the reaction wheel of SELENE. During this period, the attitude of SELENE was unstable, and the sunlight reflected at the bottom side of the body of SELENE near the SP might have become stray light. We confirmed the unstable attitude during this period from the telemetry information of SELENE. Third, the increase at $\Phi \sim 1800$ (marked B) is caused by the delay in the starting timing of the observation in a revolution, which may be due to an error in the input data for in-flight mission planning. The delay of the starting timing resulted in a short duration of the data for $i > 90^\circ$. In this case, the median value of the DN with $i > 90^\circ$ is easily affected by the reflected light at local surface features at the polar regions and the stray light.

2) NIR 1: In Fig. 7(a), the DN at $n = 115$ (NIR 1; $\lambda = 1123.8$ nm) is plotted with respect to L and i at the top axis. The DN appears to be nearly constant at $i > 90^\circ$, suggesting that the dark DN for NIR 1 can be determined in the same manner as VIS. In Fig. 7(b), the dark DN (median values of DN at $i > 90^\circ$) for $\Phi = 2041$ is plotted with respect to n. There is a large variation among n, as compared to VIS [see Fig. 6(a)]. In addition, we found that the dark DN for NIR 1 depends on the instrument temperature. In Fig. 8, the dark DNs at $n = 114$ and 115 are plotted with respect to the temperature measured by the SP1 thermometer ($T_{\rm sp1}$). The dark DN increases (or decreases) with increasing $T_{\rm sp1}$. Note that the dark DN means the dark output, which is the output from the detector when it is not illuminated by the light from the telescope, not the dark current. The level of the dark output is determined by the relative difference of dark currents between pixels and intentionally added offset. This is why some pixels show that dark DN decreases with increasing $T_{\rm sp1}$. There is also a difference in the trend between

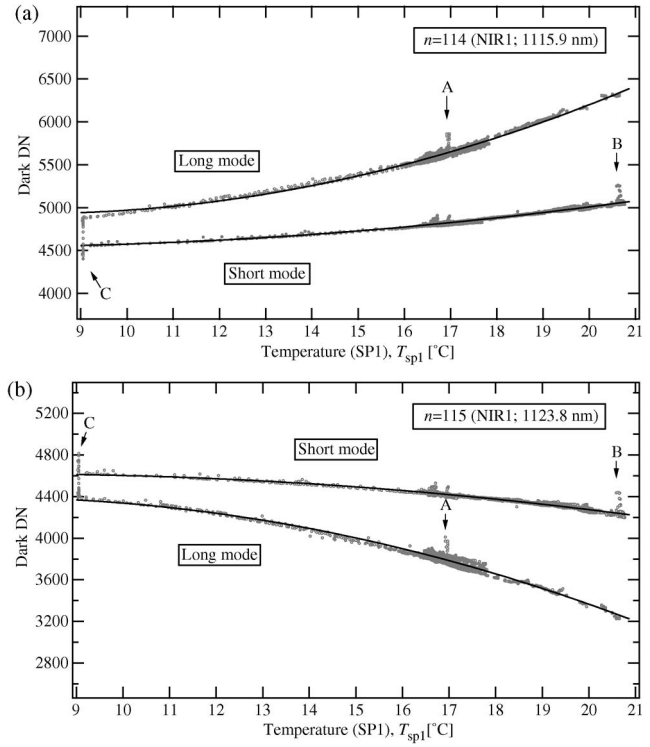

Fig. 8. Dark DN is plotted with respect to the temperature $T_{\rm sp1}$ at (a) $n = 114$ (NIR 1 #30; $\lambda = 1115.9$ nm) and (b) $n = 115$ (NIR 1 #31; $\lambda = 1123.8$ nm), respectively. The solid curves for the short exposure are the best fit curves: (a) $D_{\rm N1} = 4651 - 33.13T_{\rm sp1} + 2.550T_{\rm sp1}^2$ and (b) $D_{\rm N1} = 4494 + 32.70T_{\rm sp1} - 2.184T_{\rm sp1}^2$, respectively. The best fit curves for the long exposure are (a) $D_{\rm N1} = 5457 - 134.6T_{\rm sp1} + 8.585T_{\rm sp1}^2$ and (b) $D_{\rm N1} = 4,098 + 84.46T_{\rm sp1} - 6.054T_{\rm sp1}^2$, respectively.

the long and short exposure modes. Note that there is a vertical distribution at the lowest $T_{\rm sp1} \sim 9.05$ °C (marked C in this figure) because the lowest temperature that can be recorded is 9.05 °C. Moreover, there are temporal increases in the dark DN (e.g., A and B in the figure). These increases correspond to $\Phi \sim 1800,\ 6400,$ and 6900, where we find similar temporal increases in the dark DN in VIS [see Fig. 6(b)], which may be due to the similar cause to the VIS.

This figure reveals that the dark DN $(D_{\rm N1}(n))$ at each n can be fitted well by a quadratic equation as

$$D_{\rm N1}(n) = a_1(n) + a_2(n)T_{\rm sp1} + a_3(n)T_{\rm sp1}^2 \qquad (2)$$

where coefficients $a_1(n)$, $a_2(n)$, and $a_3(n)$ depend on the pixel number n. Using the least square fit, we determine the best fit values of $a_1(n)$, $a_2(n)$, and $a_3(n)$ for the short and long exposure modes, respectively, although we omit the data with $T_{\rm sp1} \sim 9.05$ °C. The standard deviation of the difference between the dark DN and the results obtained by (2) is 0.1%–0.3% of the typical S-value of NIR 1 (∼10 000–30 000 DN [see Fig. 3(b)]. Thus, we estimate that the error in the removal of the dark DN of NIR 1 is 0.1%–0.3% for the S-value of 10 000–30 000 DN. For the production of the L2B data, we estimate the dark DN using (2) with $T_{\rm sp1}$ measured at each observational point.

3) S-Value for Reference Sites: Fig. 3(b) shows the S-values for three reference sites. Jagged features, which were

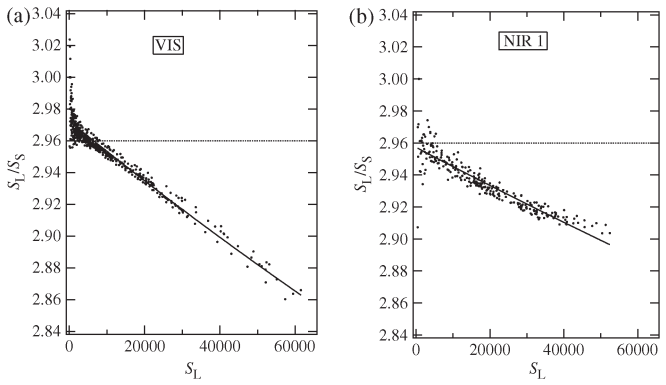

Fig. 9. $S_{\rm L}/S_{\rm S}$ are plotted with respect to $S_{\rm L}$ for (a) VIS and (b) NIR 1, respectively. The data of $S_{\rm S}$ and $S_{\rm L}$ were measured in the ground-based radiometric calibration using the integrating sphere. (a) VIS data at $n = 1$ to $n = 84$ and (b) NIR 1 data at $n = 85$ to 184 for various brightnesses of the light source are plotted. The solid curves are the best fit to (6) with $\sigma = 2.972$ and $k = 9.751 \times 10^{-7}$ (VIS) and $\sigma = 2.957$ and $k = 6.176 \times 10^{-7}$ (NIR 1), respectively. The dotted horizontal line indicates the time exposure ratio (∼2.96) between the long and short exposure modes.

observed in the original DN in NIR 1 [see Fig. 3(a)], do not appear. This indicates that the dark DN was successfully removed from the original DN in NIR 1. On the other hand, for VIS, a wavelike feature is observed at around $n = 5$–30. This is the inherent spectral feature of VIS due to the low-pass filter used to avoid the light to a wavelength of less than 500 nm.

B. Nonlinearity Correction

In order to cover the full dynamic range of SP detectors, we must take into account their nonlinear response, which indicates that the S-value is not proportional to the intensity of the input light. To examine the nonlinear response, ground-based experiments were conducted using the integrating sphere in JAXA's Tsukuba Space Center. In the experiments, we used the lamps with five different currents of 2.6, 3.3, 3.7, 3.9, and 4.8 A. The lamp sets are as follows: 1) 2.6 A × 1 lamp; 2) 3.3 A × 1 lamp; 3) 3.9 A × 1 lamp; 4) 3.3 A × 4 lamps; 5) 3.7 A × 4 lamps; 6) 3.9 A × 4 lamps; 7) 4.8 A × 4 lamps; and 8) 3.3 A × 5 lamps. We measured the S-values for the short and long exposure modes, $S_{\rm S}$ and $S_{\rm L}$, respectively, for each lamp set.

In Fig. 9, the ratios of $S_{\rm L}/S_{\rm S}$ are plotted with respect to $S_{\rm L}$ for (a) VIS ($n = 1$–84) and for (b) NIR 1 ($n = 85$–184). When $S_{\rm L} \sim 0$, $S_{\rm L}/S_{\rm S}$ is near the exposure time ratio between the short and long modes, $\sigma = 77.0/26.0 \sim 2.96$. In contrast, the ratio $S_{\rm L}/S_{\rm S}$ decreases with increasing $S_{\rm L}$. The deviation from 2.96 (horizontal dotted line) is due to the nonlinear response of the detectors.

Based on this plot, we define the nonlinearity correction equation as follows. We first assume that the true S-value after the nonlinearity correction (hereinafter S'-value) is

$$S' = S + kS^2 \qquad (3)$$

where we assume that the constant k does not depend on the wavelength. We then assume that the S'-value is proportional to the exposure time τ. In other words, the ratio of the S'-value

for the long exposure mode (S'_{L}) to that for the short exposure mode (S'_{S}) is given as

$$\frac{S'_{\mathrm{L}}}{S'_{\mathrm{S}}} = \frac{S_{\mathrm{L}} + kS_{\mathrm{L}}^2}{S_{\mathrm{S}} + kS_{\mathrm{S}}^2} = \sigma. \tag{4}$$

Introducing $x = S_{\mathrm{L}}/S_{\mathrm{S}}$, we can rewrite (4) as

$$(1 + kS_{\mathrm{L}})x^2 - \sigma x - \sigma k S_{\mathrm{L}} = 0. \tag{5}$$

Thus, we have

$$x = \sigma \frac{1 + \sqrt{1 + \frac{4kS_{\mathrm{L}}}{\sigma}(1 + kS_{\mathrm{L}})}}{2(1 + kS_{\mathrm{L}})} \tag{6}$$

where $x = S_{\mathrm{L}}/S_{\mathrm{S}} > 0$. Note that $S_{\mathrm{L}} \to 0, x \to \sigma$. When we fit the data in Fig. 9 with (6), we obtain $\sigma = 2.972 \pm 0.0004$ and $k = (9.751 \pm 0.141) \times 10^{-7}$ for VIS and $\sigma = 2.957 \pm 0.001$ and $k = (6.176 \pm 0.175) \times 10^{-7}$ for NIR 1, respectively.

If we do not take into account the nonlinearity correction, the radiance is underestimated by ∼2% (VIS) and ∼1% (NIR 1) for the S-value of 20 000 DN. The error in k would change the radiance of ∼0.01%–0.04% (VIS) and ∼0.02%–0.05% (NIR 1) for the typical S-value (10 000–30 000 DN). Thus, we estimate that the errors in the nonlinearity correction are $< \sim 0.04\%$ (VIS) and $< \sim 0.05\%$ (NIR 1), respectively.

Fig. 9(a) shows that there are two different distributions around the solid line for $S_{\mathrm{L}} > \sim 20\,000$ DN. The data above and below the solid curve correspond, for the most part, to pixels with $n > \sim 40$ and $n < \sim 40$, respectively. This may indicate that the nonlinear response depends on the pixel number. For $S_{\mathrm{L}} < 20\,000$ DN, there is no difference among n. If we determine k from only the data with $n \geq 42$ for $S_{\mathrm{L}} > \sim 20\,000$ DN, then $k = 9.813 \times 10^{-7}$. For the case of $n \leq 41$, we have $k = 9.761 \times 10^{-7}$. This difference in k would change the radiance by up to 0.03%. For the production of L2B data, we use the single k of 9.751×10^{-7} for all n in VIS.

We also see that there is a deviation from the fitting line for NIR 1, particularly at $S_{\mathrm{L}} > 40\,000$ DN. Although a cubic curve may fit better the nonlinear response for NIR 1, the difference between the present model and the cubic curve model is within the scatter of the data in Fig. 9. Therefore, we used (3) for the nonlinearity correction.

C. Wavelength Correction

In our first examination of the SP data, we did not take into account the wavelength shift. In this case, however, we observed a wavy pattern in the radiance for various observational points, particularly at lower wavelengths ($\lambda < \sim 600$ nm) in VIS. It was also shown that the amplitude of the wavy pattern varies with L in one revolution. This is thought to be due to the wavelength shift, which is defined as the deviation of the center wavelength for each pixel from the preflight value. It is also reported that there is the difference between the spectral registration by ground-based measurements and the actual behavior during flight operations in the calibration of the hyperspectral data of The Visible and Infrared Thermal Imaging Spectrometer-M on board Venus Express [8]. In this section, we describe how to quantify the wavelength shift in the S'-value. Finally, we describe a method to correct the spectral calibration according to the instrument temperature.

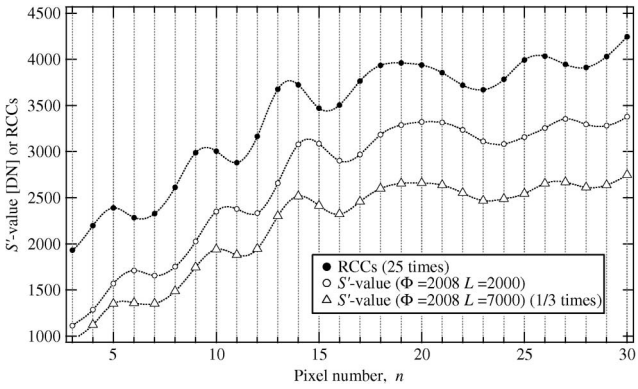

Fig. 10. Comparison between the (open circles and triangles) S'-value and (solid circles) RCCs at $n = 3$ to 30. The S'-values are obtained from the data with $\Phi = 2008$ ($L = 2000$ and $L = 7000$). In order to clarify the difference among these values, the RCCs and the S'-value at $L = 7000$ shown here are multiplied by 25 and 1/3, respectively. The dotted curves are cubic spline interpolations to determine how well S' shows the wavelength shift (see the text in detail).

1) Quantification of the Wavelength Shift: Fig. 10 shows the S'-value at $n = 3$ to 30 (at $L = 2000$ and $L = 7000$ in $\Phi = 2008$). For comparison, the RCCs are also plotted. We can see that there are wavy patterns in the S'-value and the RCCs that are due to the inherent spectral feature of the low-pass filter used in VIS. Differences in the peak positions of the wavy pattern between the S'-value and the RCCs are clear. Even in the same revolution, there is a difference in the peak position between $L = 2000$ and $L = 7000$, suggesting that the wavelength shift has short time variation. This is probably caused by the thermal distortion of the spectrometer.

In order to quantify the wavelength shift, we first interpolate the S'-value and the RCCs using the cubic spline interpolation (dotted curves in Fig. 10). Then, the ratio χ of the interpolated S' and the interpolated RCCs is calculated. Fig. 11(a) shows χ for $\Phi = 2008$ and $L = 2000$. A wavy pattern with an amplitude of $\chi \sim 0.1$, which is due to the difference in the peak position between the S'-value and the RCCs, was observed. If S' is shifted to $\epsilon = -0.87$ pixel, the amplitude of the wavy pattern in χ decreases to ∼0.01 [see Fig. 11(b)]. Therefore, in order to estimate the amount of wavelength shift, it is sufficient to find the condition (hereinafter referred to as the minimum condition) at which the amplitude of the wavy pattern in χ is the lowest.

In order to determine the minimum condition, we calculated the average χ for 250 points (2.5 pixels) before and after each point [broken curve in Fig. 11(a) and (b)]. The 250 points (2.5 pixels) correspond to the interval between the peaks of the inherent spectral feature in the S'-value and the RCCs (see Fig. 11). In order to calculate χ between the 1st and 250th points, we set χ to assume the same value for $n < 0$ as for $n = 0$. The sum $T(\epsilon)$ of the absolute difference between χ and the average χ for $n = 1 - 37$ is calculated for various pixel shifts ϵ. We then search for $\epsilon_{\min}$ at which $T(\epsilon)$ is the lowest. For the case shown in Fig. 11, $T(\epsilon)$ is the lowest at $\epsilon = -0.87$ pixel, and we estimate that the amount of the wavelength shift is $\epsilon = -0.87$ pixel ($\delta\lambda = -5.2$ nm).

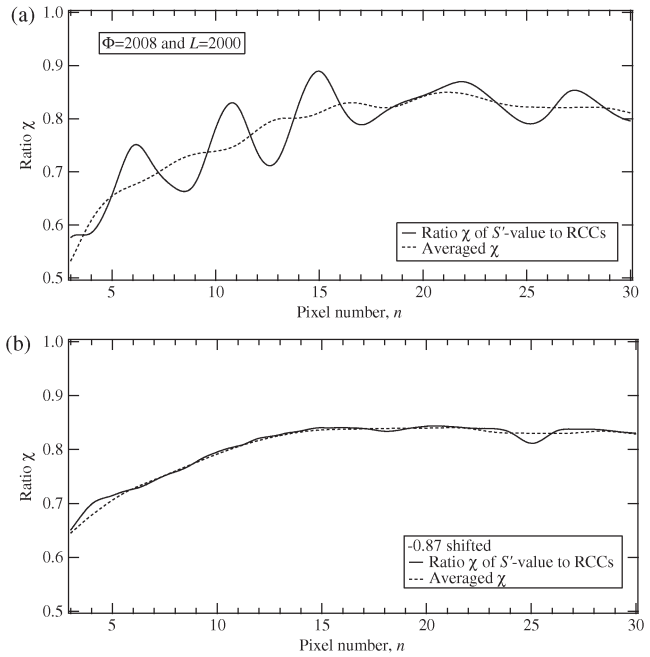

Fig. 11. (a) Ratio χ of the S'-value ($\Phi = 2008$ and $L = 2000$) to the RCCs. The broken curve is the χ averaged over 250 points (2.5 pixels) before and after each point. (b) Ratio χ and the average χ for the S'-value shifted to $\epsilon = -0.87$ pixel.

2) Temperature Dependence Model: The calculation time of the aforementioned algorithm is too long to produce L2B data from more than 68 million points. Therefore, we use the following empirical relation between the amount of the wavelength shift and the temperature of the spectrometer for the L2B production. Based on the analysis of the 14 thermometers, the SP1 thermometer was found to show the best correlation with the wavelength shift in VIS [cf., Figs. 12(c) and (d)]. Thus, we use $T_{\rm sp1}$ to estimate the amount of the wavelength shift. In Fig. 12(a), $\epsilon_{\rm min}$ determined from the aforementioned algorithm is plotted with respect to the temperature $T_{\rm sp1}$ for $\Phi = 2008$. Here, we do not use the low signal-to-noise ratio data with the maximum S' in VIS < 1500 DN because such data do not show a wavy pattern. The value of $\epsilon_{\rm min}$ is well correlated with $T_{\rm sp1}$ as

$$\epsilon_{\rm min} = q_1 + q_2 T_{\rm sp1} \tag{7}$$

where $q_1 = 3.39 \pm 0.007$ and $q_2 = -0.151 \pm 0.0004$.

A vertical distribution appears at $T_{\rm sp1} \sim 16.6$ °C. This deviation from (7) is ∼0.1 pixel (0.6 nm in wavelength). We also obtained the same vertical distribution with ∼0.1 pixels for various revolutions. The reason for this vertical distribution is as follows. The vertical distribution at $T_{\rm sp1} = 16.6$ °C is obtained from the data with $L < \sim 2000$. In Fig. 12(b), $\epsilon_{\rm min}$ and $T_{\rm sp1}$ are plotted with respect to L. For $L < \sim 2000$, $\epsilon_{\rm min}$ increases with L, while $T_{\rm sp1}$ does not change ($T_{\rm sp1} = 16.6$ °C). This makes the vertical distribution at $T_{\rm sp1} = 16.6$ °C.

In Fig. 13(a), $\epsilon_{\rm min}$ is plotted with respect to $T_{\rm sp1}$ for all Φ (every 300 lines in each Φ). It is clearly shown that there is an inflection point at $T_{\rm sp1} \sim 16$ °C. For $T_{\rm sp1} < 16$ °C, $\epsilon_{\rm min} \sim$ 0.9–1.1 ($\delta\lambda \sim$ 5–7 nm). Although the reason for this upper limit is unknown, we set $\epsilon_{\rm min} = 1.10$ pixels for $T_{\rm sp1} < 16$ °C

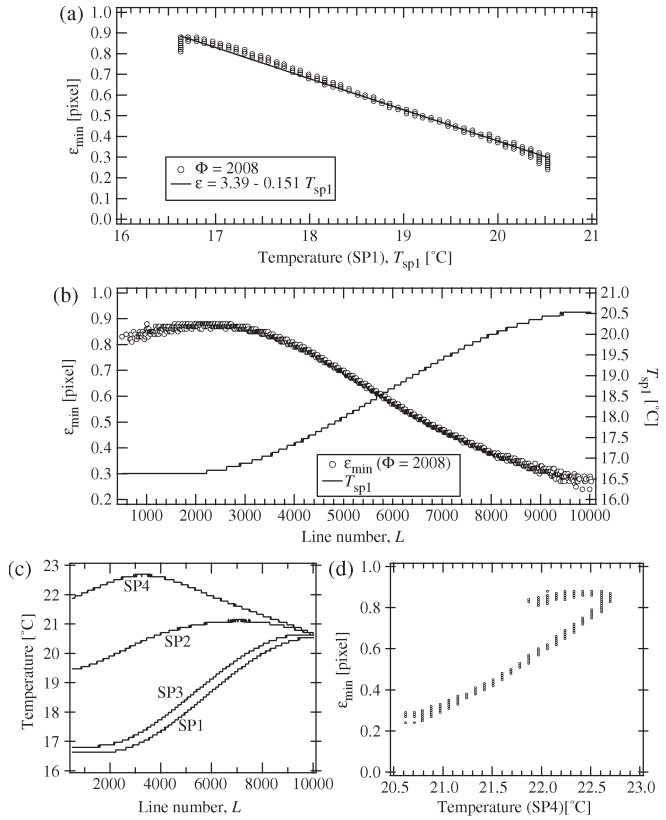

Fig. 12. (a) Amount of wavelength shift $\epsilon_{\rm min}$ is plotted with respect to $T_{\rm sp1}$ ($\Phi = 2,008$). The solid line, which represents $\epsilon_{\rm min} = (3.39 \pm 0.007) - (0.151 \pm 0.0004) T_{\rm sp1}$, is the best fit curve to the coefficient of correlation of -0.997. (b) $\epsilon_{\rm min}$ and $T_{\rm sp1}$ are plotted with respect to L. (c) Temperature variations with L of Spectrometers 1 (SP1), 2 (SP2), 3 (SP3), and 4 (SP4). (d) $\epsilon_{\rm min}$ is plotted with respect to the temperature of SP4 ($\Phi = 2008$). The correlation between $\epsilon_{\rm min}$ and the temperature of SP4 is not good.

in L2B production. Note that a vertical distribution appears at the lowest $T_{\rm sp1}$ (~ 9.05 °C) because the lowest temperature that can be recorded is 9.05 °C.

For $T_{\rm sp1} > 16$ °C, $\epsilon_{\rm min}$ decreases with increasing $T_{\rm sp1}$, but there is a large deviation, as compared to Fig. 12(a). The large deviation is partly due to the difference in $\epsilon_{\rm min}$ between the first and the last half of the mission. Fig. 13(b) and (c) shows the relation between $\epsilon_{\rm min}$ and $T_{\rm sp1}$ for $\Phi < 3300$ and $\Phi > 3300$, respectively, where $\Phi = 3300$ corresponds to the second yaw around maneuver. Most of the data for $\Phi < 3300$ are located slightly below the best fit curve (thin solid line) based on all of the data with $T_{\rm sp1} > 16$ °C [see Fig. 13(b)], while the data for $\Phi > 3300$ appear to be relatively consistent with the solid curve [see Fig. 13(c)]. Therefore, we use two empirical models for the wavelength correction for $T_{\rm sp1} \geq 16$ °C as shown at the bottom of the next page.

Based on these equations, $\epsilon_{\rm min}$ is nearly 0 when $T_{\rm sp1} \sim$ 22 °C to 23 °C, which is near room temperature for the preflight calibration experiment when the center wavelength of each detector element was determined.

For the L2B1 (and L2B2) products, $\epsilon_{\rm min}$ is calculated using (8) with $T_{\rm sp1}$ measured at each observational point. The interpolated S'-value is then shifted to $-\epsilon_{\rm min}$ pixels (hereinafter $S'_{\rm shift}$). We use the value of $S'_{\rm shift}$ at each pixel n as the S'-value after the wavelength correction [hereinafter $\hat{S}(n)$]. Note that the

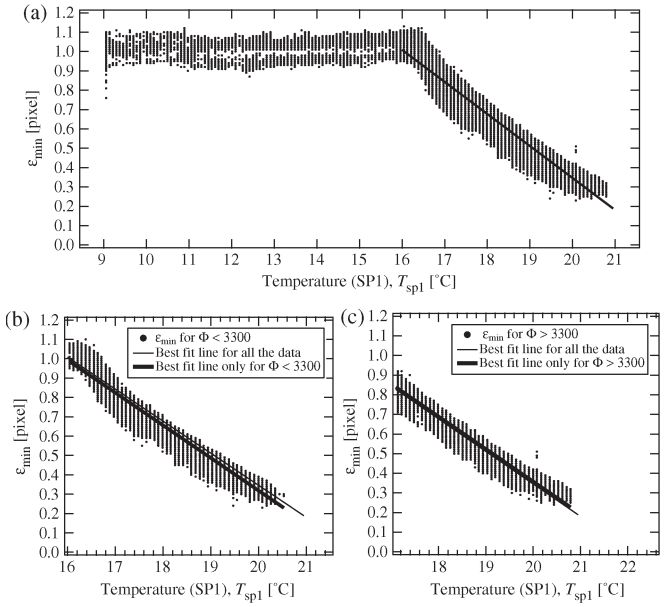

Fig. 13. (a) $\epsilon_{\min}$ for VIS is plotted with respect to T_{sp1} for all Φ (every 300 lines in each Φ). The solid line is the best fit curve for $T_{\mathrm{sp1}} > 16$ °C, which represents $\epsilon_{\min} = (3.657 \pm 0.002) - (0.166 \pm 0.0001)T_{\mathrm{sp1}}$ with the coefficient of correlation of -0.997. (b) Relation between $\epsilon_{\min}$ and T_{sp1} for $T_{\mathrm{sp1}} > 16$ °C for $\Phi < 3300$. The thin and thick solid lines are the best fit curves for all of the data and only for $\Phi < 3300$, respectively. (c) Same as (b) but for $\Phi \geq 3300$.

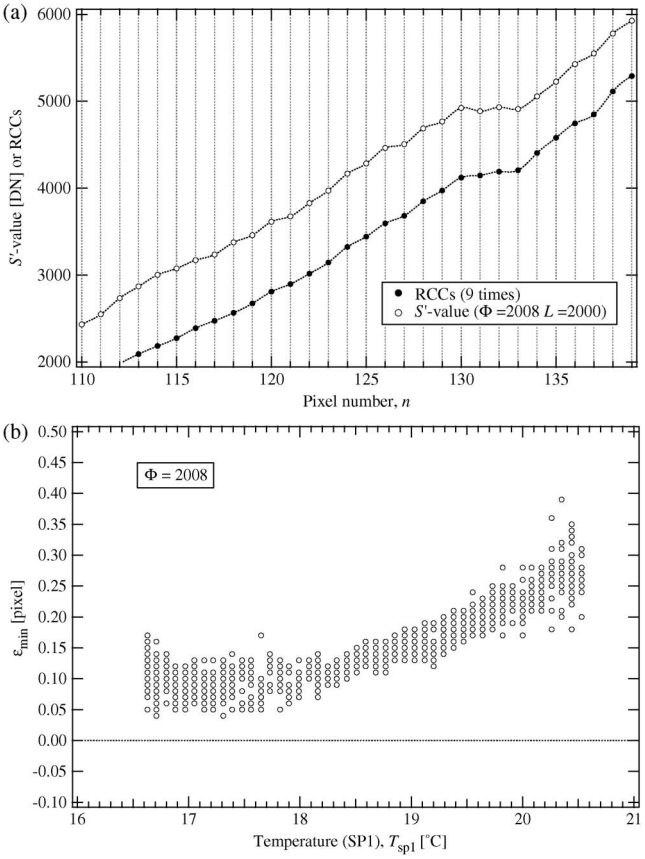

Fig. 14. (a) Comparison between the (open circles) S'-value and (solid circles) RCCs at $n = 110$ to 139. This is the case for $\Phi = 2008$ and $L = 2000$. To clarify the differences, the RCCs are multiplied by 9. (b) $\epsilon_{\min}$ is plotted with respect to T_{sp1} for NIR 1 ($\Phi = 2008$).

data of T_{sp1} show discrete distribution (i.e., step function) in Fig. 12(b). This results in an uncertainty in the estimate of T_{sp1} of up to ~ 0.09 °C. This uncertainty corresponds to the error of $\epsilon_{\min} \sim 0.015$ (0.09 nm). Moreover, the standard deviations around the empirical model (solid curve) in Fig. 13(b) and (c) are $\sim$0.04 pixel ($\delta\lambda = 0.24$ nm). Therefore, we consider the error in the wavelength correction to be $\delta\lambda = 0.3$ nm. The effect of these errors on the radiance will be discussed in Section IV-D.

3) NIR 1: The approach used to examine the wavelength shift of VIS was used to examine the wavelength shift of NIR 1. Although, unlike VIS, the RCC of NIR 1 does not have a wavy pattern, there is a depression at $n = 130$ to 138, as shown in Fig. 14(a). Thus, we determine the amount of wavelength shift in the same manner as VIS. Here, we do not use the low signal-to-noise ratio data with S' at $n = 136 < 4000$ DN because such data do not show depression features. The results are shown in Fig. 14(b). The value of $\epsilon_{\min}$ ranges from $\sim$0.10 to $\sim$0.25 for T_{sp1} of 16.5 °C to 20.5 °C, which corresponds to wavelengths of 0.8 to 2 nm. Even for various values of Φ, most of the values of $\epsilon_{\min}$ are < 0.3 pixels. In the current L2B1/L2B2 product, we do not take into account the wavelength shift in NIR 1. We consider that the error in the wavelength shift in NIR 1 is $\delta\lambda =$ 1–2 nm. The effect of this error on the radiance will be discussed in Section IV-D.

IV. Radiance Conversion

We obtain the radiance $I(n)$ from $\hat{S}(n)$ using the RCCs $C(n)$ as

$$I(n) = \frac{\hat{S}(n)}{C(n)} \tag{9}$$

where $C(n)$ was obtained in the preflight experiments for the short exposure mode. For the case of a long exposure mode, we multiplied (9) by the time exposure ratio (26.0/77.0) between the short and long exposure modes.

In Fig. 15(a), the radiance I for the three reference sites is plotted with respect to λ. An unexpected hump appears at $\lambda \sim$ 1300–1400 nm. This hump is observed not only at the three reference sites but also at other regions, indicating the inherent spectral feature in the RCCs, rather than specific spectral features of the reference sites. This is probably due to the effect of water vapor in the integrating sphere used to determine the RCCs because the preflight test was conducted under atmospheric pressure, as suggested for the Near Earth Asteroid

$$\epsilon_{\min} = \begin{cases} (3.689 \pm 0.002) + (-0.1685 \pm 0.0001)T_{\mathrm{sp1}} & \text{for } \Phi < 3300 \\ (3.668 \pm 0.002) + (-0.1655 \pm 0.0001)T_{\mathrm{sp1}} & \text{for } \Phi \geq 3300 \end{cases} \tag{8}$$

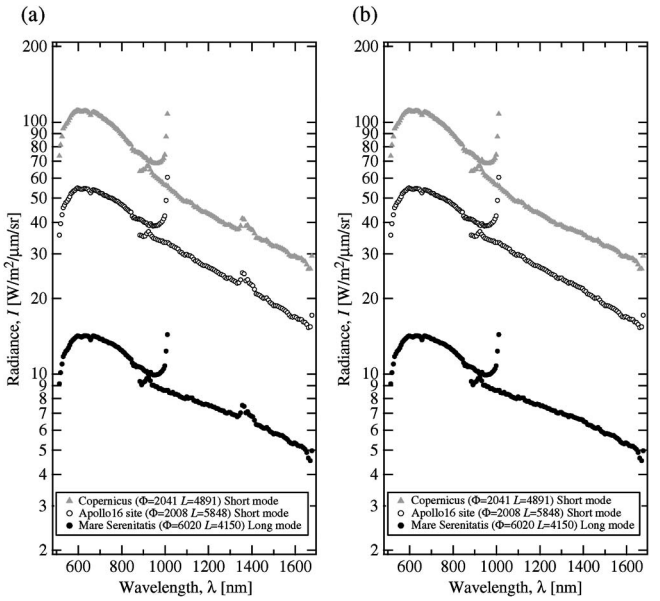

Fig. 15. (a) Radiance I is plotted with respect to the wavelength λ for the three reference sites. The hump at $\lambda \sim 1300$ to $1,400$ nm is due to the effect of water vapor. (b) Radiance I after the correction for the effect of water vapor in RCCs for the three reference sites. Note that there is no hump at $\lambda \sim 1300$ to 1400 nm.

Rendezvous mission [9]. Although the water vapor can affect other wavelengths, such as $\lambda \sim 720, 940,$ and 1140 nm, these wavelengths are not easily observable in Fig. 15(a) because the absorption at these bands is not as deep as that at $\lambda \sim$ 1300–1400 nm (e.g., [10]). In the following, we implemented a new method to remove the effect of water vapor on the RCCs only at $\lambda \sim$ 1300–1400 nm.

A. Removal of the Effect of Water Vapor on the RCCs

In order to remove the effect of water vapor on the RCCs, we use the reflectance spectra R_{62231} of Apollo 16 soil 62231 of the Reflectance Experiment Laboratory (RELAB) data, which are measured in the laboratory (e.g., [11]). First, the model radiance I_{62231} for the Apollo 16 landing site was calculated as $I_{62231} = R_{62231} \cdot F_{\odot} \cdot \cos 30^{\circ}$, where $F_{\odot}$ is the solar flux (see Section V). We then compare I_{62231} with the radiance I_{A16} measured by the SP near the Apollo 16 landing site (see Section VI). Fig. 16(a) shows that I_{A16} has a hump at $\lambda \sim 1340 - 1420$ nm, whereas I_{62231} does not. We calculate the ratio W_{A16} of I_{A16} to I_{62231} [see Fig. 16(b)]. The solid line indicates the average of W_{A16} over 25 points, which corresponds to 200 nm, before and after each point (solid line). Assuming that the deviation from the solid line results from the effect of water vapor on the RCCs, we define the ratio of W_{A16} to the averaged value (solid line) as the correction factor $\eta(n)$ of the RCCs, i.e., $C'(n) = C(n) \cdot \eta(n)$, where $C'(n)$ denotes the RCCs after the removal of the effects of the water vapor.

Using this algorithm, we determined $\eta(n)$ at $n = 143$ to 151 from the four Apollo 16 landing site observations (see Section VI). Each Apollo 16 landing site observation contains seven observational lines, but $\eta(n)$ does not depend on the precise location within the Apollo 16 landing site. The standard deviation in $\eta(n)$ is 0.02%–0.07%. In Fig. 16(c), $C'(n)$ is plotted with respect to n for NIR 1. In Fig. 15(b), the radiance based on $C'(n)$ is plotted with respect to λ. No humps are observed at 1300–1400 nm.

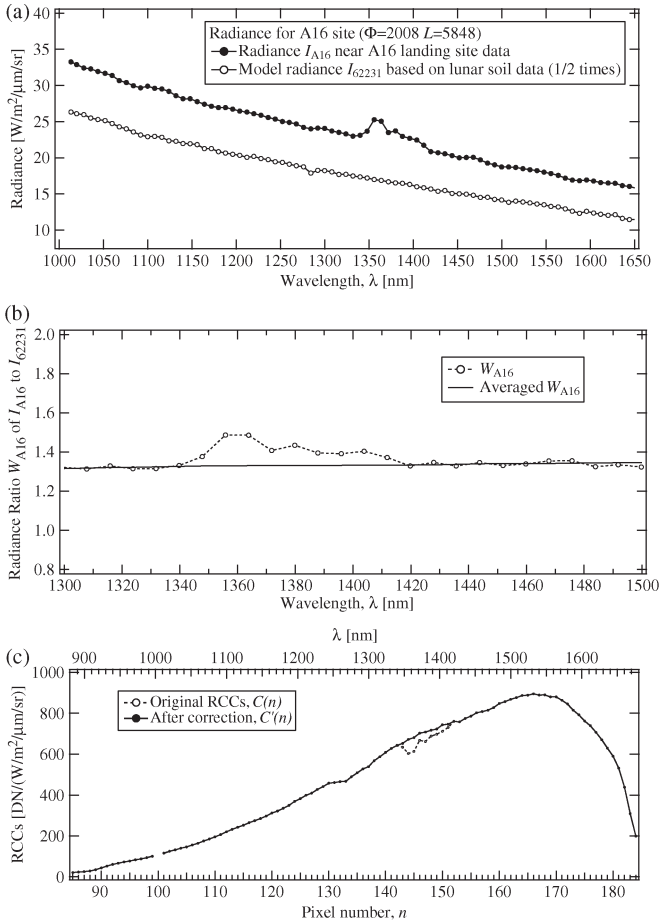

Fig. 16. (a) Comparison of the radiance (I_{A16}) of SP data near the A16 landing site based on the original RCCs and the model radiance (I_{62231}) derived from the spectral data of soil returned at the Apollo 16 landing site measured in the laboratory. Note that I_{62231} is multiplied by 1/2 because the reflectance of the A16 site based on the lunar soil data is roughly twice that of the previous Earth-based telescopic and remote-sensing observations derived by the MI (see [14]). (b) Ratio (W_{A16}) between I_{A16} and I_{62231}. The solid line was obtained by averaging W_{A16} over 25 points before and after each point. (c) Original RCCs $C(n)$ and corrected RCCs $C'(n)$ for NIR 1.

B. Out-of-Range Response

As shown in Fig. 15, there is a jump in I in the last several pixels of the VIS ($\lambda > \sim 950$ nm). This is due to the second-order light originating from the out-of-range response of the low-pass filter used in VIS. In addition, we can also see that, for NIR 1, there is a downward curve in the first several pixels ($\lambda < \sim 940$ nm) and a jump at the last pixel ($n = 184$). These pixels have low sensitivity in the NIR 1 detector at $\lambda < 950$ nm and low reflectance of the dichroic mirror. Here, we omit these data and use the data of VIS with $\lambda \leq 950.6$ nm ($n \leq 74$) and the data of NIR 1 with λ ranging from 955.4 nm ($n = 94$) to 1668.3 nm ($n = 183$). For the data with $n = 100$, which exhibited an abnormal response in the preflight experiment, we set the average value between $I(n = 99)$ and $I(n = 101)$.

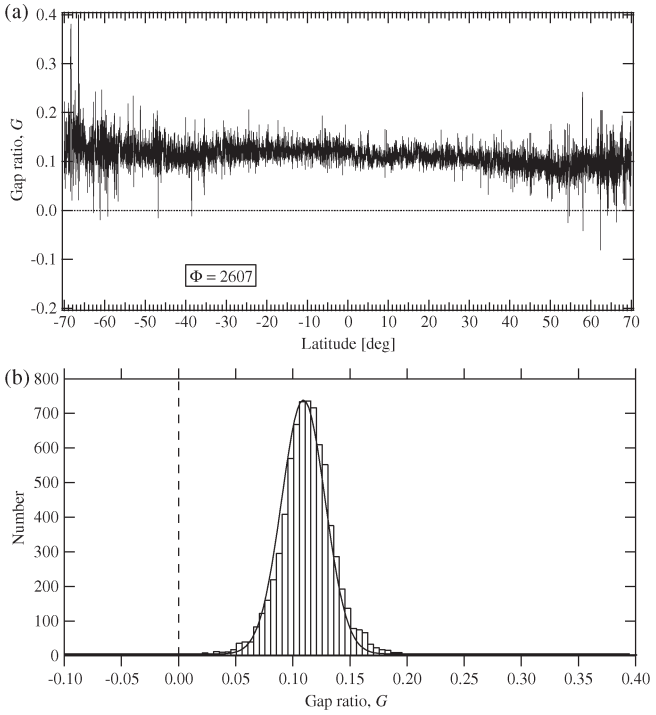

Fig. 17. (a) Gap ratio is plotted with respect to the latitude of the SP footprint, where the gap ratio is defined as $G = [I(n = 75) - I(n = 94)]/I(n = 75)$. This is the case of $\Phi = 2607$. We use the data with latitude ranging from $-70°$ to $+70°$ because the signal-to-noise ratio at high latitudes is not good. (b) Histogram of the gap ratio in (a). The solid curve is the least square fit to the Gaussian distribution: $4.83 + 733.85 \exp[-((G - 0.109)/0.0270)^2]$.

C. Gap Between VIS and NIR 1

We observed a small gap in I at the overlapping wavelengths (around $\lambda \sim 950$ nm) between VIS and NIR 1 [see Fig. 15(b)]. In Fig. 17(a), the gap ratio $G = [I(n = 75) - I(n = 94)]/I(n = 75)$ for $\Phi = 2607$ is plotted with respect to the latitude of the footprint of the SP. As shown in this figure, the gap ratio fluctuates around approximately $G \sim 0.1$. The two reasons for this gap are considered to be as follows. First, the change in the radiometric sensitivity of the detectors during/after launch may differ between VIS and NIR 1. This may account for the offset of $G \sim 0.1$. Second, the observational point of VIS is not identical to that of NIR 1 because of the small difference in sampling timing between VIS and NIR 1. The IFOV of the SP is 50×500 m. During one sampling with the IFOV, the exposure at $n = 84$ of VIS starts $\sim$4 ms later than that of NIR 1. During this interval, the SP footprint moves at $\sim$1.6 km s^{-1} on the lunar surface, resulting in a difference of $\sim$6 m in the footprint between VIS and NIR 1. In other words, the IFOV could move to $\sim$6 m. When there are horizontal variations in the radiance at several meter scales, which are due mostly to topography, the measured I in VIS could differ from that in NIR 1. This may account for the fluctuation of G. Fig. 17(b) shows a histogram of G. The distribution of G appears to follow a Gaussian distribution, which is consistent with the interpretation that the gap is due to the radiance variations in the SP's IFOV in the along-track direction.

In the present analysis, we adjusted the gap to the radiance of NIR 1. In other words, the VIS data with $n = 1$ to 84 are multiplied by $I(n = 94)/I(n = 75)$. However, the possibility exists that the low signal–noise data may result in similar values at $n = 75$ and $n = 94$ by coincidence. Thus, if $G \leq 0.01$, we use $I(n = 95)$ and $I(n = 76)$ ($\lambda = 963.5$ nm and 962.7 nm). Moreover, if $1 - I(n = 95)/I(n = 76) < 0.01$, we use $I(n = 93)$ and $I(n = 74)$ ($\lambda = 947.4$ nm and 950.6 nm). If $1 - I(n = 93)/I(n = 74) < 0.01$, we do not adjust the gap.

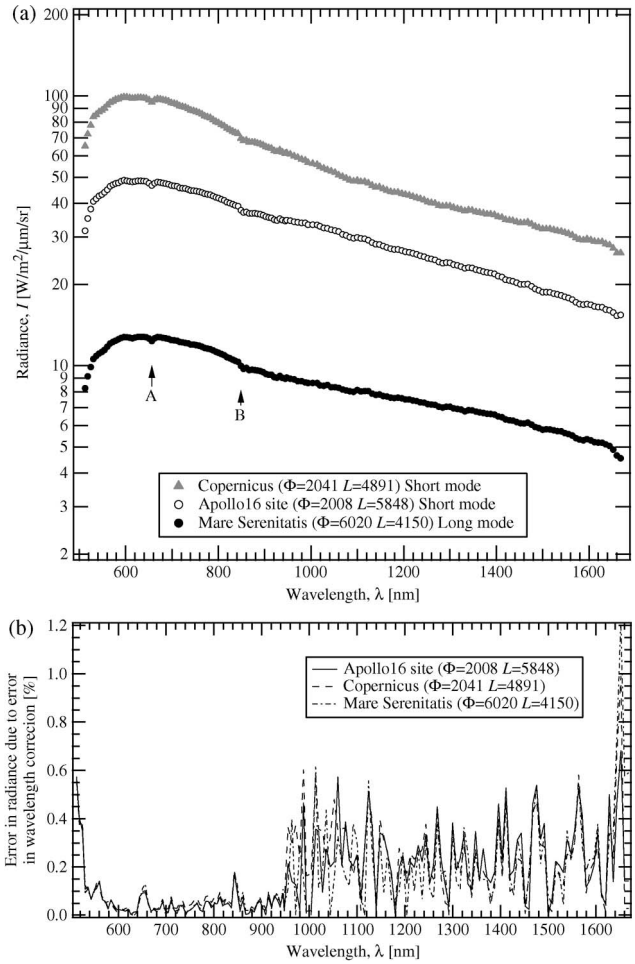

Fig. 18. (a) Radiance I after all the corrections is plotted with respect to λ for the three reference sites. The dip at $\lambda = 656$ nm (marked A) corresponds to the so-called Hα line of the Fraunhofer lines of the solar spectrum. A small gaplike feature at $\lambda = 850$ nm (marked B) is due to inherent spectral features in RCCs, which are not found in the preflight test and may have occurred during/after launch. (b) Error in the radiance due to the error in the wavelength correction.

Fig. 18(a) shows the resulting radiance after having applied the aforementioned corrections for the three reference sites. The three radiance data have peaks at $\sim$ 600–700 nm. We can see dips at $\lambda = 656$ nm (marked as A in this figure) for the three radiances, which correspond to the solar spectrum Hα line ($\lambda = 656.2$ nm) of the Fraunhofer series. Moreover, there is a gaplike feature at $\lambda = 850$ nm (marked B). This is probably due to the inherent feature in the RCCs, which may have occurred during/after launch, although this may also be due to the inherent feature in the solar data [12], [13], The inherent spectral feature at $\lambda = 850$ nm also appears in the reflectance (see Section V).

D. Error in Radiance

The various error estimates for typical S-values of 10 000–30 000 DN are summarized in Table III. The error in

TABLE III
SUMMARY OF ERROR ESTIMATES FOR RADIANCE DUE TO VARIOUS ERRORS IN RADIOMETRIC CALIBRATION

Type of error	Error in radiance [%]	
	VIS	NIR 1
Removal of dark DN	0.05 %	0.1-0.3 %
Non-linearity correction	$<\sim$ 0.04 %	$<\sim$ 0.05 %
Wavelength correction (530 nm $< \lambda <$ 1640 nm)	0.08 %	0.3 %
Wavelength correction ($\lambda <$ 530 nm or $\lambda >$ 1640 nm)	$<$ 0.6 %	$<$ 1 %
Correction of RCCs (1340 nm $< \lambda <$ 1420 nm)	-	0.02-0.07 %
Total (530 nm $< \lambda <$ 1640 nm)	$\sim$ 0.2 %†	$\sim$ 0.4-0.7 %
Total ($\lambda <$ 530 nm or $\lambda >$ 1640 nm)	$<\sim$ 0.7 %	$<\sim$ 1.4%

†For example, this error results in the uncertainty of ~ 0.0002 in reflectance for the spectrum with reflectance of 0.10.

the radiance due to the error in the wavelength correction is estimated as follows. The error in the wavelength shift was estimated to be $\delta\lambda = 0.3$ nm for VIS and $\delta\lambda =$ 1–2 nm for NIR 1. We calculate $\delta\lambda \cdot dI/d\lambda$ as the error of the radiance in the wavelength correction, where $dI/d\lambda$ was estimated from Fig. 18(a). Fig. 18(b) shows $\delta\lambda \cdot dI/d\lambda$ for the three reference sites. The error in VIS is less than 0.08%, except for the wavelength range of $\lambda < 530$ nm. For $\lambda < 530$ nm, the error is up to 0.6%. For NIR 1, the error is less than 0.3% except for the wavelength range of $\lambda > 1640$ nm. For $\lambda > 1640$ nm, the error is up to $\sim$1%. From Table III, the total error would be $\sim$0.2% in VIS and 0.4%–0.7% in NIR 1, except for $\lambda < 530$ nm and $\lambda > 1640$ nm. For the case of the edges of the wavelength range ($\lambda < 530$ nm and $\lambda > 1640$ nm), the errors are up to $\sim$0.7%–1.4%.

Some uncertainty contributions are not taken into account in the aforementioned error budget. For example, Table III does not include the relative difference between the preflight and in-flight RCCs. The relative difference between the preflight and in-flight RCCs is discussed based on the comparison in radiance between SP and MI data in [14]. In [14, Table II], we can estimate that the maximum relative difference in RCCs is $\sim$2%.

This paper did not take into account the absolute error in the RCCs, although we discussed the relative error in the radiance due to the error of the aforementioned radiometric calibration. However, if we determine the degree of space weathering from the absolute values [15] or composition analysis using the forward model with the radiative transfer modeling [16], [17], the absolute error assessment becomes important.

V. REFLECTANCE

The reflectance spectrum R is defined as the ratio of the reflected light to incident solar light, e.g., $R = I/F_{\odot}$, where $F_{\odot}$ is the solar radiance at the Moon. However, the measured radiance I depends on the observation geometry, i.e., the solar incident angle i, the emission angle e, and the phase angle g[18]. In this section, we convert the data to the reflectance

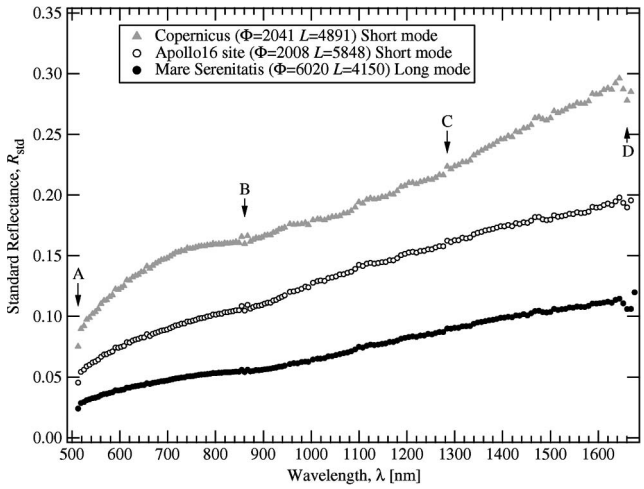

Fig. 19. Standard reflectance $R_{\rm std}$ (with $i = 30^{\circ}$, $e = 0^{\circ}$, and $g = 30^{\circ}$) for the three reference sites plotted with respect to λ. The points marked A through D indicate the inherent features in the RCCs, which are not found in the preflight test and may occur during/after launch.

in the standard geometry (referred to herein as the standard reflectance $R_{\rm std}$), with $i = 30^{\circ}$, $e = 0^{\circ}$, and $g = 30^{\circ}$, as

$$R_{\rm std}(n) = Y_{\rm std}(i, e, g, n)\frac{I(n)}{F_{\odot}(n)} \tag{10}$$

where $Y_{\rm std}(i, e, g, n)$ is the photometric correction factor to convert the data with i, e, and g into the standard reflectance. The function $Y_{\rm std}(i, e, g, n)$ is obtained from SP data by Yokota *et al.* [1]. For $F_{\odot}(n)$, we use Newkur data in MODTRAN 4 [12]. We calculate $F_{\odot}(n)$ while integrating the Newkur data with the Gaussian distribution for the sensitivity of each band n with full-widths at half-maximum of 6 nm (VIS) and 8 nm (NIR 1), where the wavelength range of the integration for each band is set to be 30 nm. For comparison, we also integrate the Newkur data with the box integration for the sensitivity with band intervals of 6 nm (VIS) and 8 nm (NIR 1), whereas the difference between the two cases is $\sim$0.2%.

TABLE IV
CONDITIONS OF THE APOLLO 16 LANDING SITE OBSERVATIONS

	1st	2nd	3rd	4th
Revolution, Φ	503	2008	4175	6375
Date	November 19, 2007	March 21, 2008	September 15, 2008	March 12, 2009
Line number range, L	4545 to 4551	5844 to 5850	4961 to 4967	5804 to 5810
†Solar Incident Angle, i	44.73°	14.84°	22.19°	25.26°
†Solar Emission Angle, e	9.84°	13.32°	2.75°	4.57°
†Solar Phase Angle, g	35.19°	26.16°	24.78°	29.83°

†The average value of 7 lines

Fig. 19 shows $R_{\rm std}$ for the three reference sites. It is shown that $R_{\rm std}$ for the three sites increases with increasing λ. The absolute value of $R_{\rm std}$ differs among the three sites. The value of $R_{\rm std}$ for the Mare Serenitatis is ∼1/2 and ∼1/3 lower than that for the Apollo 16 landing site and Copernicus crater, respectively. The lunar mare is composed primarily of basalt lava, which has a lower albedo than the other regions, such as highland regions.

We find that there are inherent spectral features in the three $R_{\rm std}$, as indicated by B and C in this figure. We also observe the same features in the reflectance for other observational sites, suggesting that these features are due to the inherent spectral feature in the RCCs, which may have been caused during/after launch. In addition, there are sudden drops in $R_{\rm std}$ at $\lambda \sim 510$ nm (marked A) and 1650 nm (marked D). As mentioned earlier, this is probably due to the low signal-to-noise ratio data at the edges of the wavelength in the low-pass filter for VIS and the dichroic mirror for NIR 1.

With respect to the error in $R_{\rm std}$, there are two types of errors. The first is due to the error in $F_{\odot}(n)$, which was estimated earlier to be 0.2%, and the second results from the photometric correction, which is described by Yokota *et al.* [1].

VI. DISCUSSION: APOLLO LANDING SITE OBSERVATION

The Apollo 16 landing site is used for the radiometric calibration of U.S. Clementine data (e.g., [19]–[21]). This is partly because of its well-characterized geologic setting and the existence of samples having spectral reflectance that was measured at RELAB (e.g., [11]). We selected the Apollo 16 landing site as the radiometric calibration test site of the SP and the MI and conducted four Apollo 16 landing site observations periodically (hereinafter ASO). The four ASOs were conducted at six-month intervals: November 19, 2007 (first ASO), March 21, 2008 (second ASO), September 15, 2008 (third ASO), and March 12, 2009 (fourth ASO). In each observation, SELENE tilted its attitude (roll-cant maneuver) to attain the condition with a phase angle of $g \sim 30°$. The photometric conditions for the four ASOs are summarized in Table IV. In this section, we compare the four ASOs to examine the stability of the SP during the mission period.

The target area of the Apollo 16 sites for the second ASO was selected by Ohtake *et al.* [14]. The image of the target area is shown in Fig. 20. We also use the same target region for the first, third, and fourth ASOs. In order to select L, which covers the target region, we used SP L2C data, which provide the positions of the SP footprints on the accompanying MI image (see [14]). The ranges of L for the four ASOs are listed in Table IV. Each ASO contains seven consecutive footprints spanning ∼3.5 km.

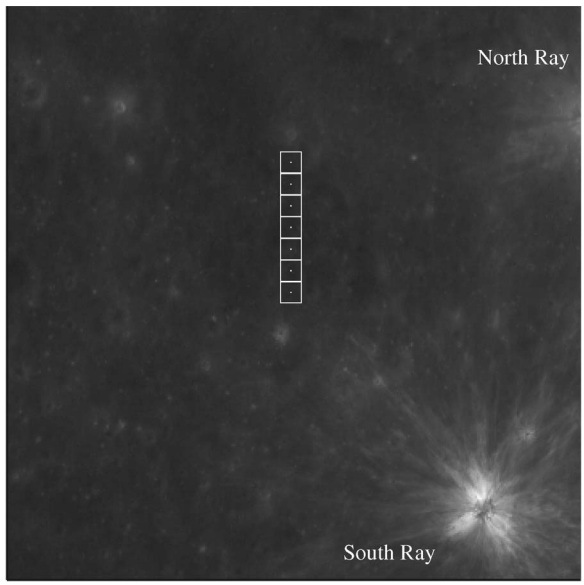

Fig. 20. Location of the second observation of the Apollo 16 landing site observation (second ASO). The image was taken by MI. The seven white rectangles denote the SP footprint in the target regions of the ASO. In this observation, the SP footprint moves from the top to the bottom of the image.

A. Comparison in Radiance

Fig. 21(a)–(d) shows I for the four ASOs. There are differences in I within each ASO. The maximum differences within each ASO are ∼20% (first ASO), ∼5% (second), ∼15% (third), and ∼17% (fourth). The difference in I within each ASO is partly due to an inhomogeneous surface albedo or topography in this area [14].

Fig. 22(a) shows the comparison of the four ASOs, where seven I values for each ASO are averaged. The average I values differ among the four ASOs. As will be shown later, however, we consider that this difference is explained by the difference in geometric conditions among the four observations

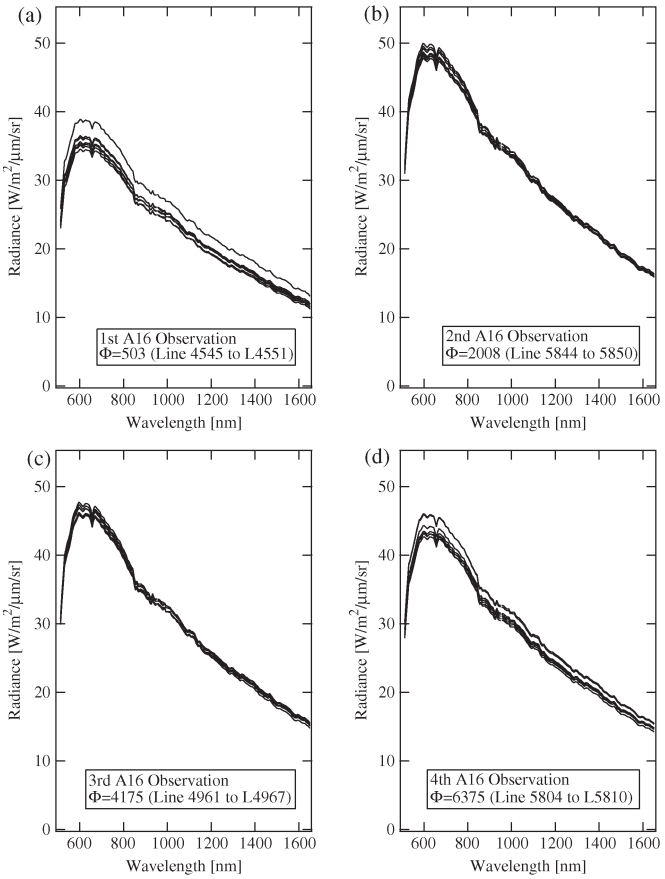

Fig. 21. Radiance I for four Apollo 16 landing site observations.

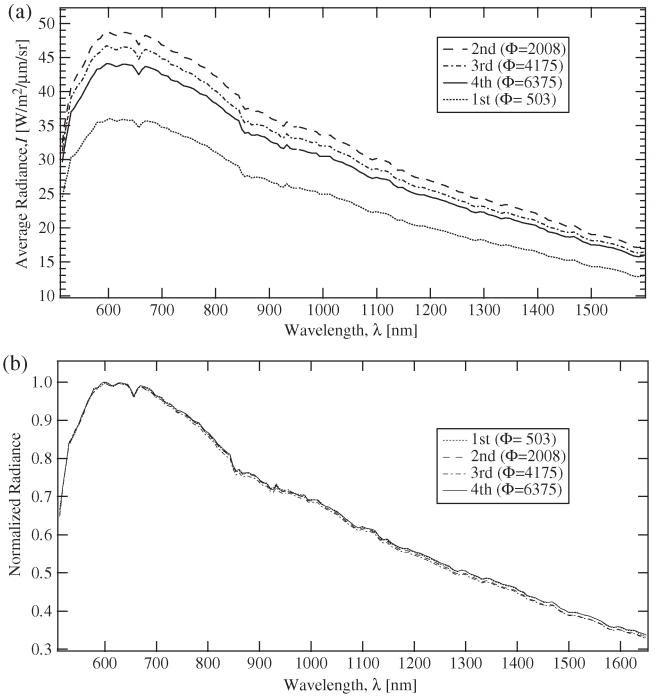

Fig. 22. (a) Average radiance for each Apollo 16 landing site observation. (b) Normalized average radiance, where the average radiance I in (a) is divided by the maximum value of I at $\lambda \sim 600$ nm.

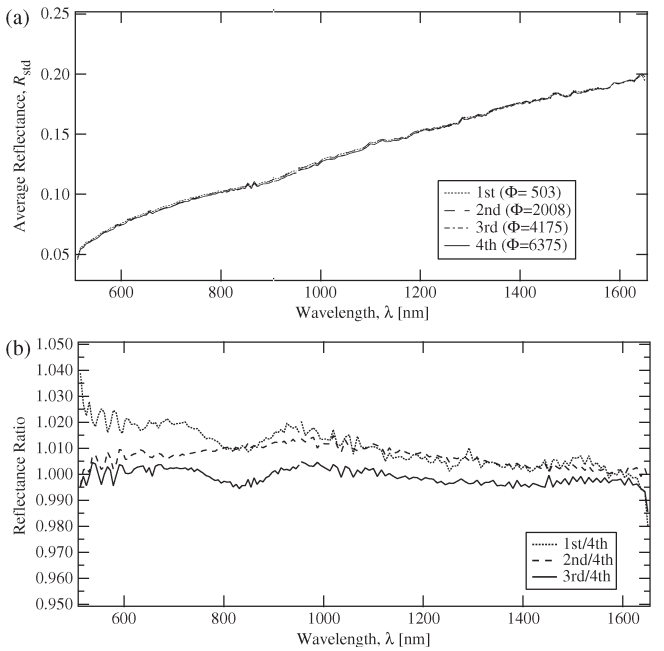

Fig. 23. (a) Average reflectance for each Apollo 16 landing site observation. (b) Reflectance ratios of the first, second, and third ASOs to the fourth ASO.

(see Table IV). Indeed, the normalized radiance in Fig. 22(b), which was divided by the maximum value at ∼600 nm for each average I, exhibits a similar radiance pattern, with differences of ∼0.5%–0.8%.

B. Comparison in Reflectance

After having applied the photometric correction described in [1] to the data shown in Fig. 21, we calculate the standard reflectance $R_{\rm std}$ for the four ASOs. Fig. 23(a) shows the comparison of the four ASOs, where seven $R_{\rm std}$ values for each ASO are averaged. The absolute value and slope of $R_{\rm std}$ are similar among the four ASOs. Fig. 23(b) shows the $R_{\rm std}$ ratios of the first, second, and third ASOs to the fourth ASO. The ratios do not vary significantly with λ. The average values of these ratios are 1.011 ± 0.011 (first/fourth), 1.007 ± 0.004 (second/fourth), and 0.999 ± 0.005 (third/fourth), respectively. In Table V, we also compare the average $R_{\rm std}$ at $\lambda = 602.5, 950.6, 1252.0,$ and 1603.7 nm, with the standard error among seven observational lines as the error. Table V shows that the typical difference in the average $R_{\rm std}$ among the four ASOs is ∼0.4%–1.1%. On the other hand, the typical differences in the average $R_{\rm std}$ within each ASO are ∼1.0%–1.9% (first ASO), ∼0.5%–0.7% (second), ∼0.4%–0.6% (third), and ∼1.0%–1.2% (fourth), respectively. Therefore, the differences in $R_{\rm std}$ among the four ASOs are within the typical differences within each ASO. We thus conclude that the degradation of SP is not significant over the mission period within the differences due to an inhomogeneous surface albedo or topography in this area.

VII. SUMMARY

This paper focused on the radiometric calibration of VIS and NIR 1 (0.5–1.7 μm) of the SP to retrieve the reflectance for the mineralogical survey. In this calibration, we proposed new methods for the nonlinearity correction, the wavelength

TABLE V
REFLECTANCE AT FOUR APOLLO 16 LANDING SITE OBSERVATIONS

Wavelength	Average R_{std} for seven lines			
λ [nm]	1st	2nd	3rd	4th
602.5	0.0763 ± 0.0008	0.0751 ± 0.0005	0.0747 ± 0.0004	0.0747 ± 0.0009
950.6	0.1194 ± 0.0018	0.1191 ± 0.0005	0.1179 ± 0.0005	0.1175 ± 0.0012
1252.0	0.1564 ± 0.0026	0.1570 ± 0.0006	0.1557 ± 0.0008	0.1562 ± 0.0016
1603.7	0.1926 ± 0.0037	0.1928 ± 0.0009	0.1920 ± 0.0011	0.1928 ± 0.0021

correction, and the correction of the RCCs in the water-vapor-affected spectral region. The nonlinear response was characterized based on the preflight data, and the nonlinearity correction would increase the radiance by a few percent. We also developed the method to quantify the wavelength shift using the inherent spectral feature in the VIS data and the RCCs. Since the amount of the wavelength shift in VIS appears to depend on the temperature of the spectrometer, we implemented the temperature dependence model to correct the wavelength shift. As for the removal of the effects of water vapor on RCCs, we compared the SP data near the Apollo 16 landing site with the laboratory spectra of soil returned from the Apollo 16 site.

After all of the radiometric corrections, including the photometric correction, we finally obtained the reflectance spectra for the three reference sites. We found several inherent spectral features in the reflectance for various reference sites, suggesting that the RCCs at several pixels may have changed during/after launch. Based on the comparison of the four Apollo 16 site observations (ASOs), we examined the stability of the radiometric calibration. The difference in reflectance after the photometric correction is $\sim$0.4%–1.1%, which is within the standard error in the reflectance within each ASO. Therefore, we concluded that the degradation of SP is not significant over the mission period within the differences due to an inhomogeneous surface albedo or topography in this area.

ACKNOWLEDGMENT

The authors would like to thank Y. Yamamoto of Japan Aerospace Exploration Agency (JAXA) for his support in conducting the optical experiment at JAXA's Tsukuba Space Center. The authors would also like to thank Fujitsu Ltd., JASCO Corporation, and Mitsubishi Space Software Company, Ltd., for their dedicated efforts in developing the Spectral Profiler instrument and its ground data system.

REFERENCES

[1] T. Yokota, T. Matsunaga, M. Ohtake, J. Haruyama, R. Nakamura, S. Yamamoto, Y. Ogawa, T. Morota, C. Honda, K. Saiki, K. Nagasawa, K. Kitazato, S. Sasaki, A. Iwasaki, H. Demura, and N. Hirata, "Refinement of lunar Vis/NIR phase curve acquired by SELENE Spectral Profiler," in *Proc. 41st Lunar Planet. Sci.*, 2010, vol. 1533, p. 2532.

[2] T. Matsunaga, M. Ohtake, J. Haruyama, and H. Otake, "A visible and near infrared spectrometer for Selenological and Engineering Explorer (SELENE): Performance and calibration requirements from scientific objectives," *J. Remote Sens. Soc. Jpn.*, vol. 19, no. 5, pp. 490–507, 1999.

[3] T. Matsunaga, M. Ohtake, J. Haruyama, Y. Ogawa, R. Nakamura, Y. Yokota, T. Morota, C. Honda, M. Torii, M. Abe, T. Nimura, T. Hiroi, T. Arai, K. Saiki, H. Takeda, N. Hirata, S. Kodama, T. Sugihara, H. Demura, N. Asada, J. Terazono, and H. Ohtake, "Discoveries on the lithology of lunar crater central peaks by SELENE Spectral Profiler," *Geo. Res. Lett.*, vol. 35, p. L23 201, 2008.

[4] J. Haruyama, T. Matsunaga, M. Ohtake, T. Morota, C. Honda, Y. Yokota, M. Torii, and Y. Ogawa, "Global lunar-surface mapping experiment using the Lunar Imager/Spectrometer on SELENE," *Earth Planets Space*, vol. 60, no. 4, pp. 243–255, 2008.

[5] R. Nakamura, T. Matsunaga, Y. Ogawa, S. Yamamoto, T. Hiroi, K. Saiki, N. Hirata, T. Arai, K. Kitazato, H. Takeda, T. Sugihara, S. Kodama, M. Ohtake, J. Haruyama, and Y. Yokota, "Ultramafic impact melt sheet beneath the South Pole–Aitken basin on the Moon," *Geo. Res. Lett.*, vol. 36, no. 22, p. L22 202, Nov. 2009, DOI: 10.1029.2009GL040765.

[6] S. Yamamoto, R. Nakamura, T. Matsunaga, Y. Ogawa, Y. Ishihara, T. Morota, N. Hirata, M. Ohtake, T. Hiroi, Y. Yokota, and J. Haruyama, "Possible mantle origin of olivine around lunar impact basins detected by SELENE," *Nat. Geosci.*, vol. 3, no. 8, pp. 533–536, Aug. 2010, DOI:10.1038/NGE0897.

[7] S. Kodama, M. Ohtake, Y. Yokota, A. Iwasaki, J. Haruyama, T. Matsunaga, R. Nakamura, H. Demura, N. Hirata, T. Sugihara, and Y. Yamamoto, "Characterization of Multiband Imager aboard SELENE: Preflight and inflight radiometric calibration," *Space Sci. Rev.*, vol. 154, no. 1–4, pp. 79–102, Jul. 2010, DOI 10.1007/s11214-010-9661-z.

[8] A. C. Moinelo, G. Piccioni, E. Ammannito, G. Filacchione, and P. Drossart, "Calibration of hyperspectral imaging data: VIRTIS-M onboard Venus Express," *IEEE Trans. Geosci. Remote Sens.*, vol. 48, no. 11, pp. 3941–3950, Nov. 2010.

[9] N. R. Izenberg, J. F. Bell, J. W. Warren, S. L. Murchie, K. Peacock, E. H. Darlington, B. Carcich, C. Chapman, B. E. Clark, A. Harch, G. Heyler, J. Joseph, P. Martin, L. McFadden, B. Merline, M. Robinson, J. Veverka, and D. Wellnitz, "In-flight calibration of the Near Earth Asteroid Rendezvous mission's near infrared spectrometer," *Icarus*, vol. 148, no. 2, pp. 550–571, Dec. 2000.

[10] R. O. Green, M. L. Eastwood, C. M. Sarture, T. G. Chrien, M. Aronsson, B. J. Chippendale, J. A. Faust, B. E. Pavri, C. J. Chovit, M. Solis, M. R. Olah, and O. Williams, "Imaging spectroscopy and the Airborne Visible/Infrared Imaging Spectrometer (AVIRIS)," *Remote Sens. Environ.*, vol. 65, no. 3, pp. 227–248, Sep. 1998.

[11] C. M. Pieters, "LPI contribution 980," in *Proc. New Views of the Moon II: Understanding the Moon through the integration of diverse datasets*, Flagstaff, AZ, Sep. 1999, pp. 22–24.

[12] C. A. Gueymard, "The sun's total and spectral irradiance for solar energy applications and solar radiation models," *Solar Energy*, vol. 76, no. 4, pp. 423–453, Apr. 2004.

[13] S. D. Miller and R. E. Turner, "A dynamical lunar spectral irradiance data set for NPOESS/VIIRS day/night band nighttime environmental applications," *IEEE Trans. Geosci. Remote Sens.*, vol. 47, no. 7, pp. 2316–2329, Jul. 2009.

[14] M. Ohtake, T. Matsunaga, Y. Yokota, S. Yamamoto, Y. Ogawa, T. Morota, C. Honda, J. Haruyama, K. Kitazato, H. Takeda, A. Iwasaki, R. Nakamura, T. Hiroi, S. Kodama, and H. Otake, "Deriving the absolute reflectance of lunar surface using SELENE (Kaguya) Multiband Imager data," *Space Sci. Rev.*, vol. 154, no. 1–4, pp. 57–77, Jul. 2010.

[15] P. G. Lucey, G. J. Taylor, and E. Malaret, "Abundance and distribution of iron on the moon," *Science*, vol. 268, no. 5214, pp. 1150–1153, May 1995.

[16] P. G. Lucey, "Mineral maps of the moon," *Geophys. Res. Lett.*, vol. 31, p. L08 701, 2004, DOI:10.1029/2003GL019406.

[17] B. Hapke, "Space weathering from Mercury to the asteroid belt," *J. Geophys. Res., E*, vol. 106, no. E5, pp. 10 039–10 073, 2001.
[18] B. Hapke, *Theory of Reflectance and Emittance Spectroscopy (Topics in Remote Sensing)*. Cambridge, U.K.: Cambridge Univ. Press, 1993.
[19] E. Eliason, C. Isbell, E. Lee, T. Becker, L. Gaddis, A. McEwen, and M. Robinson, "The Clementine UVVIS global lunar mosaic," Clementine UVVIS Digital Image Model CD1997.
[20] S. Tompkins and C. M. Pieters, "Mineralogy of the lunar crust: Results from Clementine," *Meteor. Planet. Sci.*, vol. 34, no. 1, pp. 25–41, Jan. 1999.
[21] C. M. Pieters, J. W. Head, III, L. Gaddis, B. Jolliff, and M. Duke, "Rock types of South Pole–Aitken basin and extent of basaltic volcanism," *J. Geophys. Res.*, vol. 106, no. E11, pp. 28 001–28 022, 2001.

Satoru Yamamoto received the Ph.D. degree in planetary sciences from Kobe University, Kobe, Japan, in 1999.

He is currently a Research Associate with the Center for Global Environmental Research, National Institute for Environmental Studies, Tsukuba, Japan.

Dr. Yamamoto is a member of the Japanese Society of Planetary Sciences and the Remote Sensing Society of Japan.

Tsuneo Matsunaga received the Ph.D. degree in engineering from the University of Tokyo, Tokyo, Japan, in 1997.

He is currently the Chief of Office for Global Environmental Database with the Center for Global Environmental Research, National Institute for Environmental Studies (NIES), Tsukuba, Japan.

Dr. Matsunaga is a member of the NIES Greenhouse gases Observating SATellite project and the Japan–U.S. Advanced Spaceborne Thermal Emission and Reflection Radiometer Science Team and is the Principal Investigator of the Spectral Profiler instrument on board the Japanese lunar explorer Kaguya.

Yoshiko Ogawa received the Ph.D. (Doctor of Science) degree from the Department of Earth and Planetary Science, University of Tokyo, Tokyo, Japan, in 2002.

Since 2009, she has been an Assistant Professor with the Research Center for Advanced Information Science and Technology (CAIST), The University of Aizu, Aizu-Wakamatsu, Japan. She is interested in morphology and mineralogy of terrestrial planets, particularly Mars and the Moon, deep space exploration programs and remote sensing of planetary surfaces for understanding the environment and its evolution, and computational study (data analysis and numerical simulation) to understand the physical process, particularly focusing on Martian hydrology.

Ryosuke Nakamura received the Ph.D. degree in planetary sciences from Kobe University, Kobe, Japan, in 1996.

He was a Research Associate with Kobe University from 1996 to 2000 and an Invited Researcher with the Japan Aerospace Exploration Agency, Sagamihara, Japan, from 2000 to 2004. He is currently a Researcher with the Information Technology Research Institute, National Institute of National Institute of Advanced Industrial Science and Technology, Tsukuba, Japan.

Dr. Nakamura is a member of the Japanese Society of Planetary Sciences and the Astronomical Society of Japan.

Yasuhiro Yokota received the Dr.Sc. degree from the University of Tokyo, Tokyo, Japan, in 2002.

He is currently a Research Associate with National Institute for Environmental Studies (NIES), Tsukuba, Japan.

Dr. Yokota is a member of the NIES Greenhouse gases Observating SATellite project and the Lunar Imager/Spectrometer team of the Japanese lunar explorer Kaguya.

Makiko Ohtake received the Ph.D. degree from Tohoku University, Sendai, Japan, in 1997.

She is currently an Assistant Professor with the Institute of Space and Astronautical Science/Japan Aerospace Development Agency, Sagamihara, Japan, and the Principal Investigator of the Multiband Imager on board the Japanese lunar orbiter Selenological and Engineering Explorer (Kaguya).

Junichi Haruyama received the Ph.D. degree from Kyoto University, Kyoto, Japan, in 1994.

From 1996, he worked for the development of the Terrain Camera, the Multiband Imager, and the Spectral Profiler on board the Japanese lunar orbiter Selenological and Engineering Explorer (Kaguya). He is currently the Principal Investigator of the Terrain Camera and is also involved in a lot of Japanese and international lunar and planetary missions as a Co-Investigator or an adviser. He is currently an Assistant Professor with the Institute of Space and Astronautical Science/Japan Aerospace Development Agency, Sagamihara, Japan. He is also a Visiting Associate Professor of Kumamoto University, Kumamoto, Japan, and The University of Aizu, Aizu-Wakamatsu, Japan.

Dr. Haruyama is a lunar and planetary scientist.

Tomokatsu Morota received the Ph.D. degree in science from Kanazawa University, Kanazawa, Japan, in 2003.

He is a Research Fellow of the Research In SElenodesy Project, National Astronomical Observatory of Japan (NAOJ), and is a Co-Investigator of Lunar Imager/Spectrometer working group for Japanese lunar explorer Kaguya.

Chikatoshi Honda received the Dr.Sc. degree from the Kyushu University, Fukuoka, Japan, in 2005.

He is currently an Assistant Professor with the Research Center for Advanced Information Science and Technology (CAIST), The University of Aizu, Aizu-Wakamatsu, Japan. He is interested in planetary morphology such as crater and volcanic feature. He was a member of the Kaguya project from 2006 to 2008.

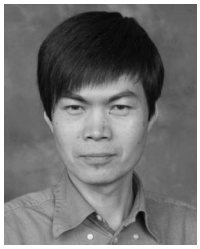

Takahiro Hiroi received the Ph.D. degree in mineralogy from the University of Tokyo, Tokyo, Japan, in 1988, specializing in mineralogical remote sensing of asteroids and meteorites in the context of solar system formation and evolution.

He is currently a Senior Research Associate with Brown University, Providence, RI. He operates in the Reflectance Experiment Laboratory, a National Aeronautics and Space Administration-funded multiuser laboratory, wherein visible, near-infrared, and infrared reflectance spectra of extraterrestrial and terrestrial geologic materials are measured and analyzed. He is also engaged in experimental and modeling studies of spectral mixing models and space weathering and applies his expertise to space missions such as Hayabusa and Kaguya.

Shinsuke Kodama received the B.S., M.S., and Ph.D. degrees from the Nagoya University, Nagoya, Japan, in 1999, 2001, and 2004, respectively.

He is currently a Researcher with the Information Technology Research Institute, National Institute of Advanced Industrial Science and Technology, Tsukuba, Japan.

Dr. Kodama is a member of the Lunar Imager/Spectrometer on board the Japanese lunar explorer Kaguya.